Supplementary Information for
Total Absorption Photoabsorber (TAP) of Sunlight

Hai-Lung Wang[1,2,3,5★], Man Liu[2,3,5], Lei Miao[4★], and Xinjun Li[1]
[1]CAS Key Laboratory of Renewable Energy, Guangzhou Institute of Energy Conversion, Chinese Academy of Sciences, Guangzhou, 510640, PR China
[2]University of Chinese Academy of Sciences, Beijing, 100049, PR China
[3]School of Physics and Electronic Engineering, Taishan University, Taian, 271000, PR Chain
[4]Guangxi Key Laboratory of Information Material, Guangxi Collaborative Innovation Center of Structure and Property for New Energy and Materials, School of Material Science and Engineering, Guilin University of Electronic Technology, Guilin 541004, China
[5]These authors contributed equally: Hai-Lung Wang, Man Liu
★E-mail: wanghl@ms.giec.ac.cn; miaolei@guet.edu.cn.

This PDF file includes:

Supplementary Information Text

Methods

Materials

Silver nitrate （$AgNO_3$） was purchased from Sinopharm Chemical Reagent Co., Ltd.. Tetraethyl orthosilicate (TEOS) was purchased from DAMAO CHEMICAL REAGENT FACTORY. Ethanol and formaldehyde solution (37-40%) were purchased from Guangzhou Chemical Reagent Factory. Iron ion (Fe (II) and trisodium citrate dihydrate were purchased from TIANJIN FUCHEN CHEMICAL REAGENTS FACTORY. Poly(vinylpyrrolidone) (PVP, Mw=30000 g/mol, the concentration was calculated in terms of repeating unit) was purchased from Aladdin. Ultrapure deionized (DI) water was prepared by ULUPURE (UPK-I-5T，resistivity 18.2 MΩ·cm). All chemicals at a given analytical grade were used as received without further purification.

Synthesis of SiO_2 nanospheres

The silica nanospheres were synthesized using the classic Stöber method[73] with minor modifications. Typically, the mixture of 3.17 ml TEOS and 25 mL DI water maintained vigorously stirring, another mixture including 2.52 ml (25%) ammonium hydroxide ($NH_3 \cdot H_2O$), 1.8 ml DI water, and 25 ml ethanol was added in one portion, vigorously stirred for 30 min, then gently stirred for hydrolysis at 50 ℃. After hydrolysis reaction undergoing 3 hour, the product was collected by centrifugation at 5000 rpm, removed the supernatant, the precipitate was washed with ethanol three times and dried in the oven at 105 ℃. The final product of SiO_2 nanospheres (I-1#) were with diameter about 190-210 nm. It is available to tune the diameter by varying the dosage and molar ratios of reactant and the reaction temperature. Using 3.78 ml TEOS and reacted at ambient temperature, other terms were employed under some conditions with the above sample, and got the SiO_2 nanospheres (I-2#) were with diameter about 210-230 nm.

Synthesis of SiO_2-Ag

0.72 g SiO_2 nanospheres (I-1#) was dispersed into 30 ml DI water, added 30 ml, iron ion (Fe (II) (0.15 M), vigorously stirred for 1 hour. The suspension was centrifuged at 5000 rpm, and washed three times with DI water. The precipitate was redispersed into 30 ml DI water, and vigorously stirred 10 min. Added 15 ml fresh silver ammonia solution (0.175 M) and vigorously stirred and reacted 1hour under intermittent ultrasonic suspension uniformity. The product was collected by centrifugation at 5000 rpm and washed three times with DI water, and then redispersed in 30 ml DI water or ethanol. The colloid suspension of SiO_2-Ag (II-1#) was on shelf under ambient condition. The colloid suspension of SiO_2-Ag (II-2#) was fabricated by the same process, except that the reaction time was 2 hours at 50-60 ℃.

Synthesis of TAP of sunlight

85 mg silver nitrate (precursor) was added in 200 ml aqueous solution containing 0.25wt % PVP, then the concentration of silver nitrate was 2.5 mM, stirred 5-10 min.

6 ml colloid suspension of SiO_2-Ag (II-1#) and 1 ml trisodium citrate dehydrate solution (0.06 M) were added the above solution, vigorously stirred 10 min to ensure the mixture was definitely homogeneous dispersion system, dropwise added 150 μl formaldehyde

solution. After reacted 2 hours, gently stirred for shells ripening 9 hours in water bath of 75 ℃. The precursor was reduced and silver atoms grown along with seeds involving Ag nanocrystals and coated the core of SiO_2-Ag, and finally covered the core with the shape of shape the closed arranged bee-eyes shells. The TAP (III-1#) were centrifuged at 4000 rpm and washed in succession with DI water and ethanol for three times, then redispersed in 30 ml DI water with 3.6×10^{13} photoabsorbers/L. The colloid suspension of TAP (III-1#) was on shelf under ambient condition. The colloid suspension of TAP (III-2#) was fabricated by the same process, except that using 3.75 mM $AgNO_3$ and the shell ripening time was 12 hours.

Test the overall performances of generating solar steam via TAP of sunlight under the natural sunlight

The colloid suspension of TAP handled by shake, transferred a certain volume of this suspension (the exact volume depended on the designed concentration of TAP) to a 25 ml beaker (volume more than 36 ml) and diluted with DI water, and stirred well. The dispersion of TAP has strong, ultrabroadband and full-range plasmonic resonances absorption spectra, that is TAP. The dispersion was directly illuminated with sunlight focused by Fresnel lens (harvesting irradiation area: 35 × 35 cm, sunlight transmittance: 88-93%, focal length: 37 cm). In outdoor experiments, the irradiation area on the dispersion interface was about 1.7-2.2 cm in spot diameter, which means that the optical concentration ratio was 253-423× times, and the average optical concentration ratio was ~300x times which was low concentrated solar radiation. Measured the initial and terminal temperature and weigh of bulk dispersion, intensity of sunlight, duration, and local time for evaluating the overall performances of generating solar steam. The batch of outdoor tests include Section I-IV which conducted by varying the concentration of the TAP (III-1#). The TAP concentration of Section I-IV was $\sim 7 \times 10^{12}$, $\sim 1.2 \times 10^{13}$, 1.8×10^{13}, and $\sim 2.4 \times 10^{13}$ photoabsorbers/L, respectively. The sets of outdoor tests employed by TAP (III-2#) used $\sim 2 \times 10^{13}$ photoabsorbers/L, which overall performances correspond to Figure 6. Note that, for quickly and accurately evaluate the overall performances of generating solar steam via TAP, all the outdoor tests of generating solar steam under sunlight irradiation did not take any insulation measure. As the outdoor tests, the intensity of sunlight and the ambient temperature, and the relative humidity were in range of 300-1000 W/m^2, and 18-30 ℃, respectively, and the relative humidity was more than 50%.

Test the macroscopic temperature of hot-spots involving the stacking TAP

Here we in-situ measured the macroscopic temperature of hot-spots in terms of TAP stacking on the substance of glass via real-time recording by thermal infrared imaging (IR camera). First, it needs to adjust the IR camera focusing till clearly present the profiles of small beakers, then putted two cleaned slices microscope slides (thickness: 1.0-1.2 mm) on the small beakers, dropwise added DI water on the microscope slides. To ensure precisely measure the temperature distribution, adjusted the focusing again before the subsequent tests. In the first test, irradiated the DI water on the microscope slide more than 60 s as the blank control test, observed the temperature and whether generate steam or not. Dropwise added 20 droplets (~1 ml) suspension of TAP into the DI water, then irradiated with focused sunlight, the intensity of natural sunlight ranging from 701 to 776 W/m^2. The dispersion fast heated up to boiling temperature and generated rapid steam and

macroscopic bubbles in 3.4 s, after DI water was exhausted through evaporating steam, continue to irradiate the stacking TAP, the macroscopic temperature of hot-spots of stacking TAP skyrocketed to made the glass break to pieces in 4.3s, corresponding to maximum of 510.99 ℃ (Figure S22a,b). The second test was the same as the above, except that used 27 drops/droplets (~1.35 ml) suspension of TAP into the DI water, recorded the maximum of 621.48 ℃ (Figure S22a,c). The whole course is shown in Supplementary Video1, and the curves of temperature distribution and the capture of macroscopic temperature involving hot-spots were shown in Figure S22.

Characterization

Glancing Angle X-ray diffractometer (GAXRD, PANalytical X'pert Pro MPD) operated at 40 KV and 40 mA, using Cu-Ka radiation (λ= 1.54 Å), field emission scanning electron microscopy (FESEM, S-4800, Hitachi Japan), transmission electron microscopy (TEM, JEM-2010F) equipped with an energy-dispersive spectrometer (EDS, Thermo) attachment, ultraviolet-visible-near-infrared spectrophotometer (UV-vis-NIR, Lambda 950, PerkinElmer), Atomic Force Microscope (AFM, Multimode 8, Bruker), Solar Power Meter (PC-2, Jinzhou Sunshine Technology Co. Ltd), IR camera (E60, FLIR), thermogravimetry (TG, STA 409 PC, NETZSCH).

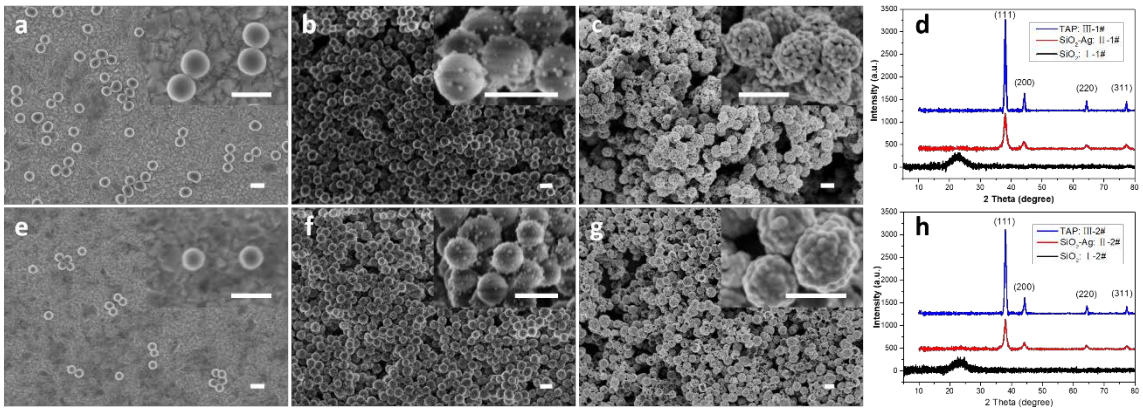

Figure 1. The fabricating samples of TAP.

a-c, the SEM image of SiO_2 (I-1#), SiO_2-Ag (II-1#), and TAP (III-1#), respectively. d, XRD pattern of the fabricating samples of TAP including SiO_2 (I-1#), SiO_2-Ag (II-1#), and TAP (III-1#). e-g, the SEM image of SiO_2 (I-2#), SiO_2-Ag (II-2#), and TAP (III-2#), respectively. **h**, XRD pattern of the fabricating samples of TAP including SiO_2 (I-1#), SiO_2-Ag (II-1#), and TAP (III-1#). Both the final product of TAP including III-1# and III-2# with a fac-centered cubic (fcc) structure (ICSD collection code: 064994) were nothing more than pure element of silver without introducing impurity. View form the intensity ratio between (200) and (111) diffraction peaks (**d**,**h**), both the TAP including III-1# and III-2# are inherently abundant in the most stable (111) plane of fcc silver shells resulting in the crystallographic configuration stability. In each case, the scale bar is equal to 300 nm.

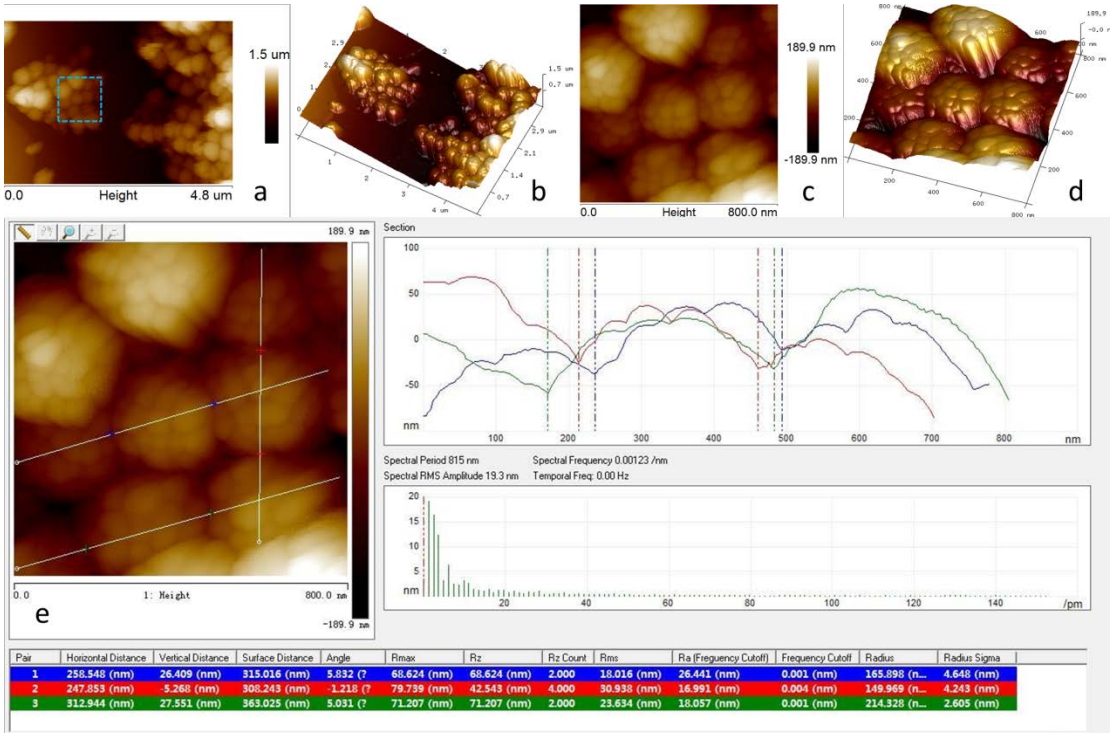

Figure 2. The AFM images of geometrical properties in terms of the closed arranged bee-eyes shells of TAP.

a, The low magnification 2D AFM image of TAP (III-2#) show the closed arranged bee-eyes shells. **b**, The low magnification AFM topography image correspond to (**a**). **c**, The high magnification 2D AFM image of TAP (III-2#), which zoom in the region of (**a**) has been marked with the dotted box with blue color in (**a**), shows the closed arranged bee-eyes shells. **d**, The high magnification AFM topography image correspond to (**c**). **e**, The section line-scanned 2D AFM image of TAP corresponding (**c**) shows closed arranged bee-eyes spherical assembly shells. The measured TAP had been stored under ambient condition more than 33 months before employed AFM measurement.

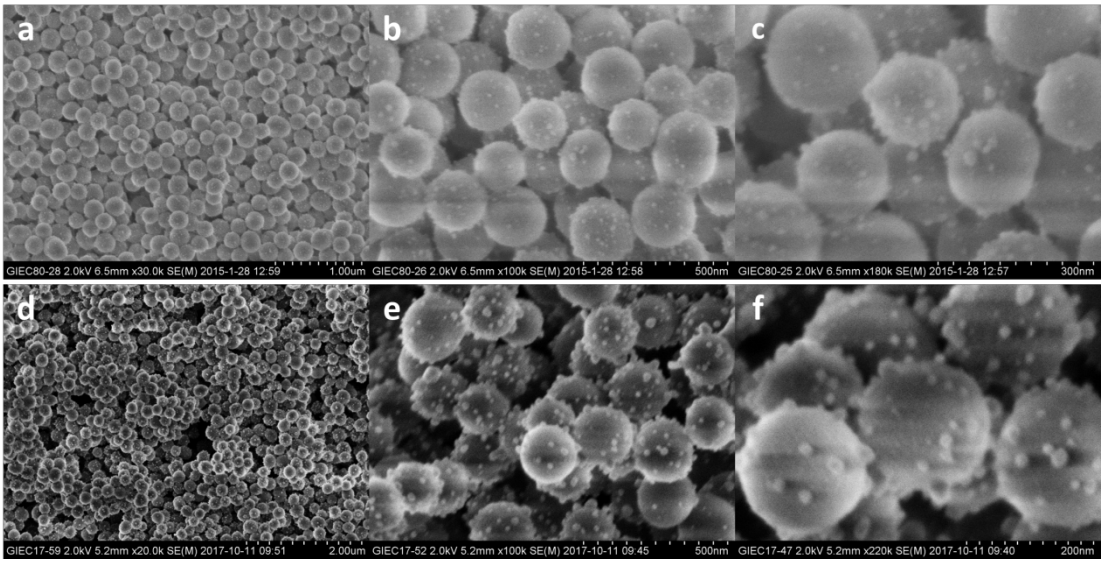

Figure 3. The SEM images of long-term stability in terms of SiO_2-Ag (II-1#).

a-c, the SEM image of initial SiO_2-Ag ranging from low magnification to high magnification. **d-f**, the SEM image of long-term stored SiO_2-Ag ranging from low magnification to high magnification. The highly loaded nanocrystals of SiO_2-Ag covered the interfaces of SiO_2, and shows long-term stability due to partial nanocrystals firmly embedded into the internal of amorphous SiO_2 core. The shelf-life duration was more than 33 months.

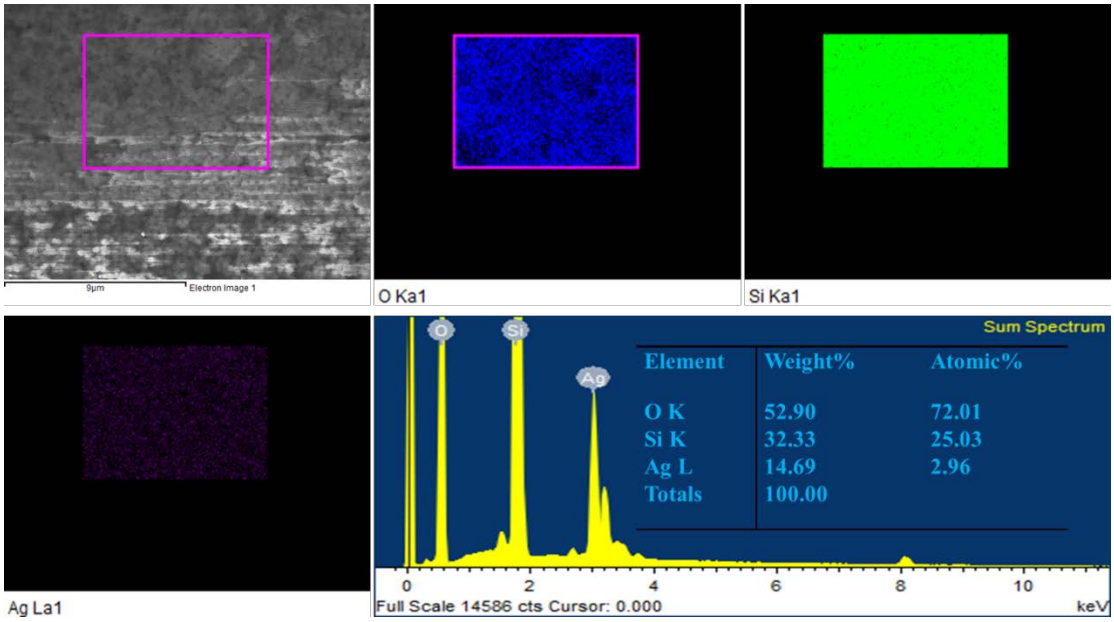

Figure 4. The SEM-EDS images of long-term stability and highly loaded nanocrystals in terms of SiO_2-Ag (II-1#).

The measured SiO_2-Ag dispersion had been stored under ambient condition more than 33 months before employed EDS measurement. The element content of silver demonstrates the highly loaded nanocrystals covered on the interfaces of SiO_2.

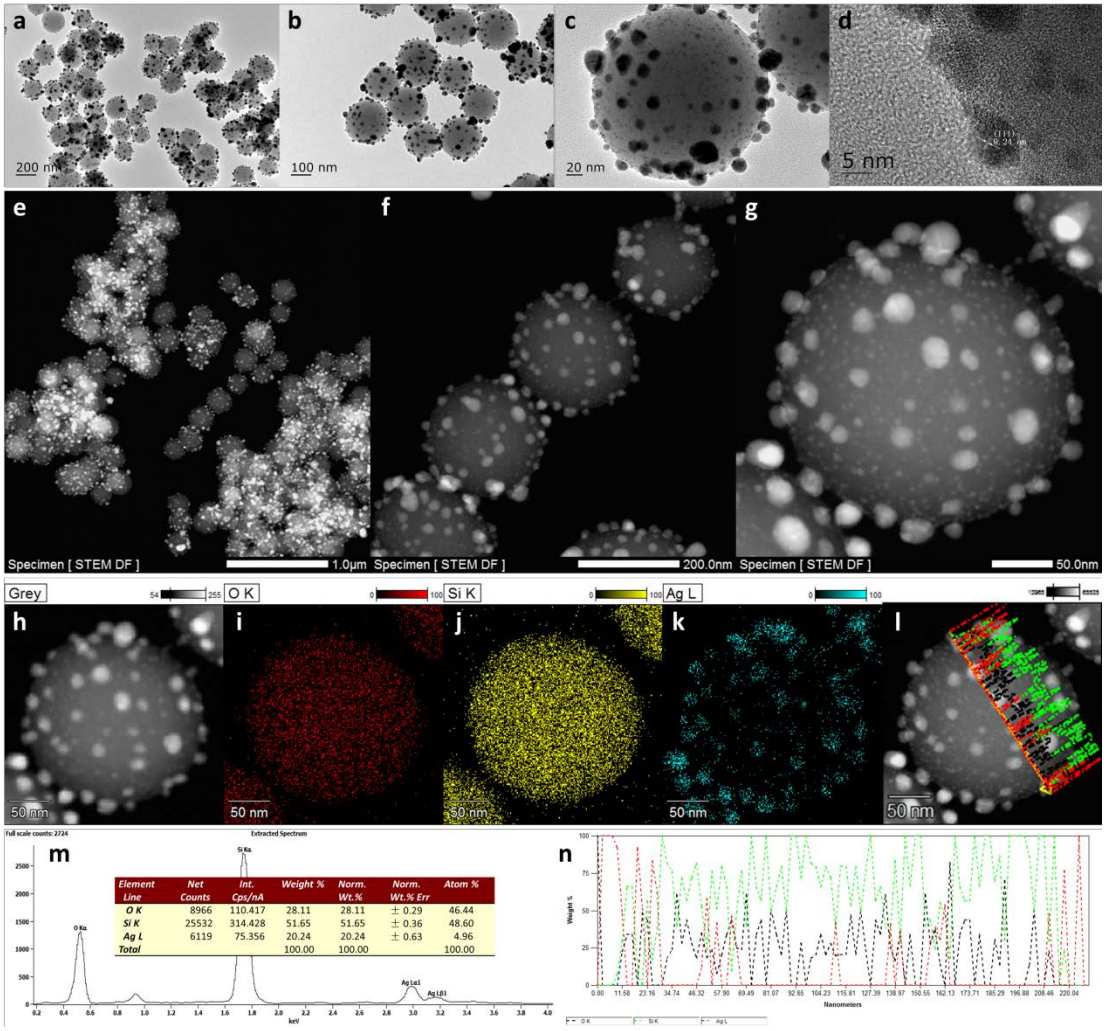

Figure 5. The TEM images of long-term stability and highly loaded nanocrystals in terms of SiO_2@Ag (II-1#).

a-c, TEM image of SiO_2Ag (II-1#) from low magnification to high magnification. The measured SiO_2-Ag dispersion had been stored under ambient condition more than 33 months before employed measurements. As the seeds for epitaxial growth of shells, the highly loaded nanocrystals of SiO_2-Ag covered the interfaces of SiO_2 and are helpful to the epitaxial growth of shells in the process of synthesis TAP. **d**, The high-resolution TEM (HRTEM) image of nanocrystals on the core of SiO_2. Partial nanocrystals firmly embedded into the internal of amorphous SiO_2 core. The well-resolved interference fringe spacing of 0.24 nm corresponds to the interplanar distance between the (111) planes. **e-g**, HAADF-STEM images from low magnification to high magnification. The diameter of cores and the nanoceystals on the core are in range of 190-210 nm, and 3-25 nm, respectively. **h-k**, Energy dispersive X-ray (EDX) elemental mapping of (**h**). **l**, The area-normalized line-scanned elemental intensity profiles of (**h**). **m**, The Energy dispersive X-ray spectrometer (EDS) of the individual TAP of (**h**), the inset shows the details of element contents. **n**, The indicated lines corresponding to (**l**), the black line, green line, and the red line correspond to O, Si, and Ag, respectively.

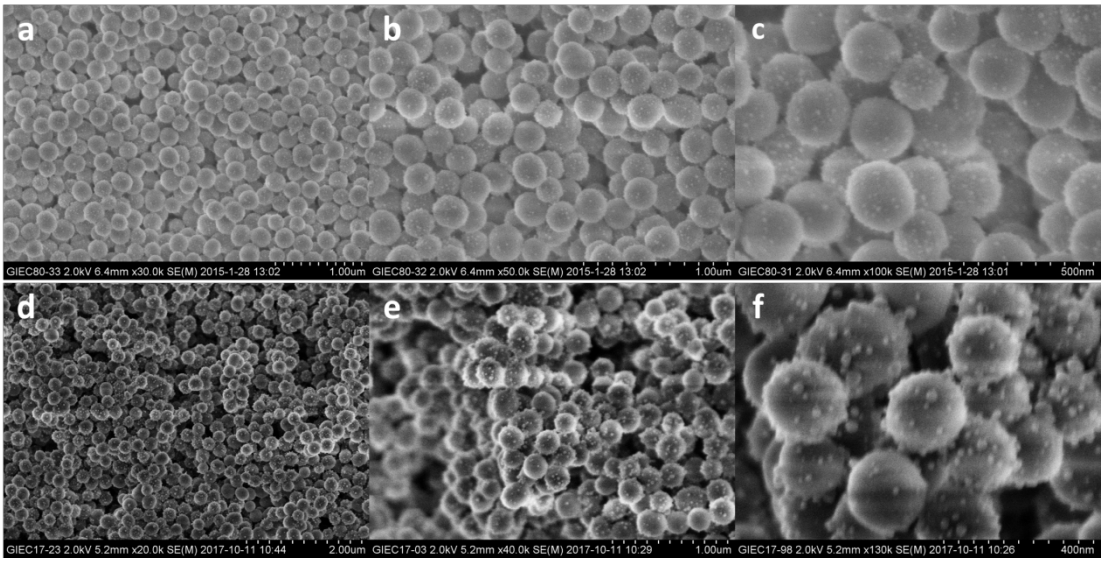

Figure 6. The SEM images of long-term stability in terms of SiO_2-Ag (II-2#).

a-c, the SEM image of initial SiO_2-Ag ranging from low magnification to high magnification. **d-f**, the SEM image of long-term stored SiO_2-Ag ranging from low magnification to high magnification. The highly loaded nanocrystals of SiO_2-Ag covered the interfaces of SiO_2, and shows long-term stability due to partial nanocrystals firmly embedded into the internal of amorphous SiO_2 core. The shelf-life duration was more than 33 months.

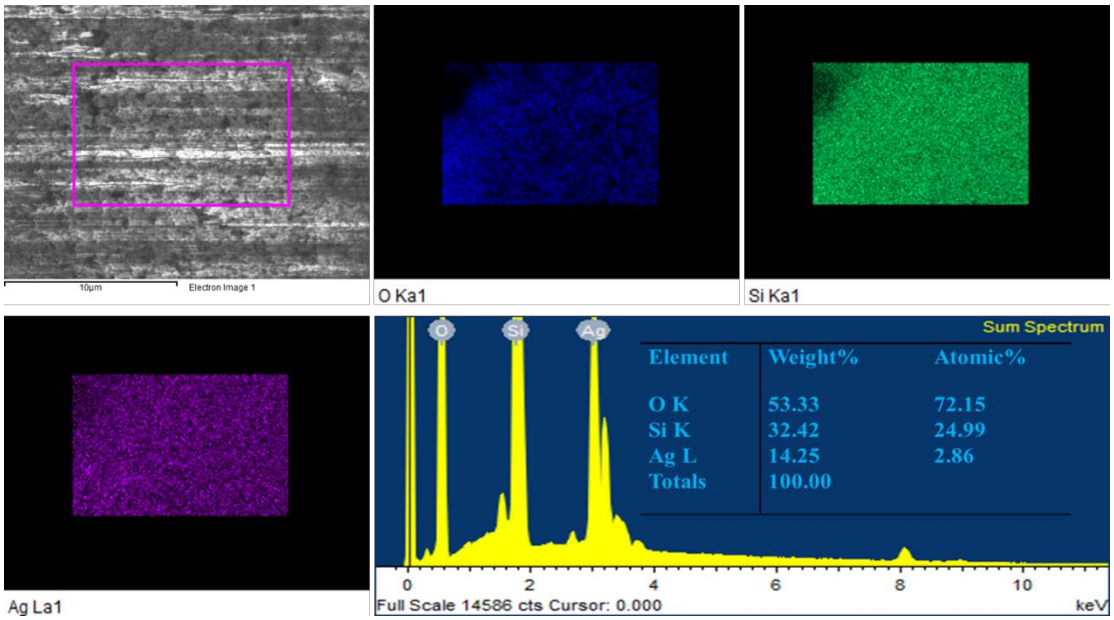

Figure 7. The SEM-EDS images of long-term stability and highly loaded nanocrystals in terms of SiO_2-Ag (II-2#).

The measured SiO_2-Ag dispersion had been stored under ambient condition more than 33 months before employed EDS measurement. The element content of silver demonstrates the highly loaded nanocrystals covered on the interfaces of SiO_2.

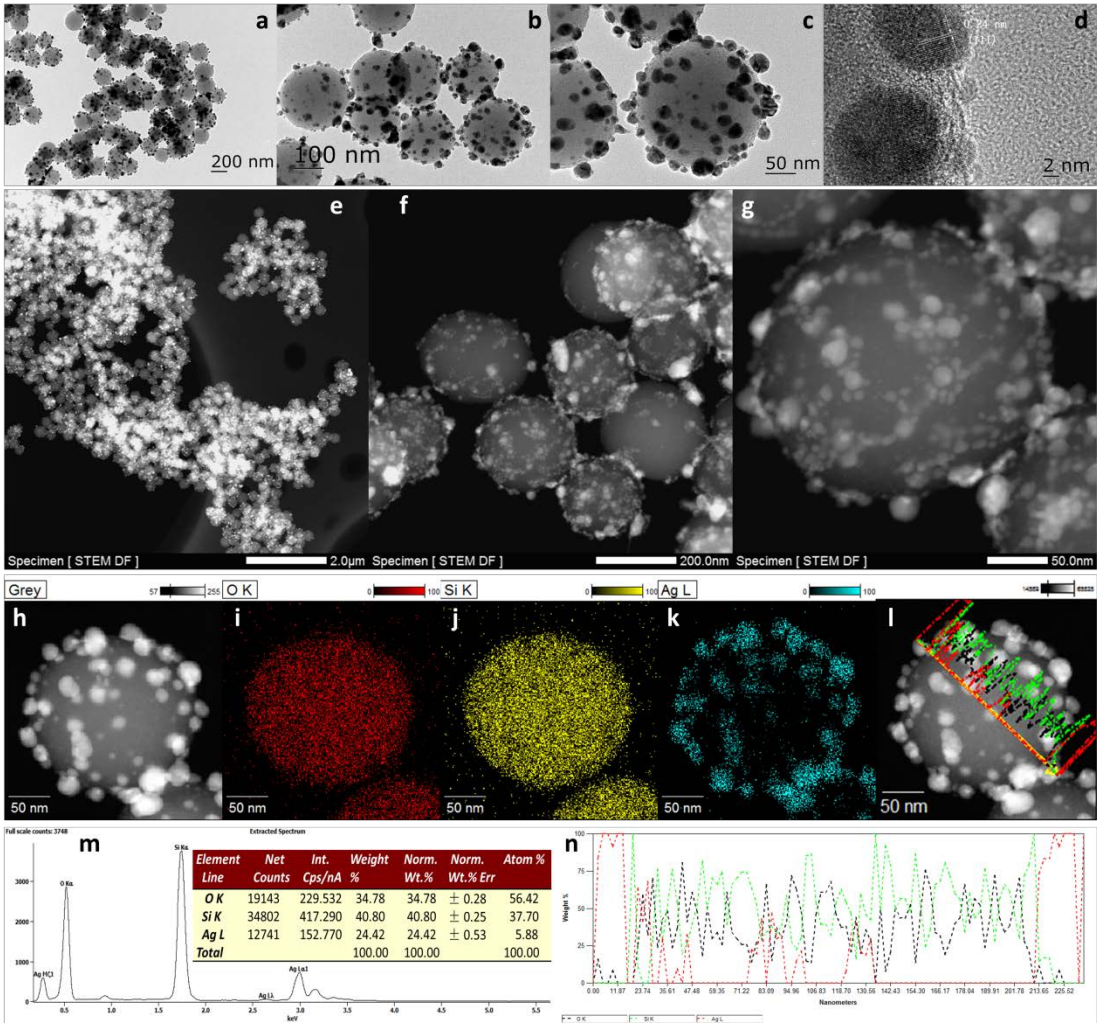

Figure 8. The TEM images of long-term stability and high loaded nanocrystals in terms of SiO_2@Ag (II-2#).

a-**c**, TEM image of SiO_2-Ag (II-1#) from low magnification to high magnification. The measured SiO_2-Ag dispersion had been stored under ambient condition more than 33 months before employed measurements. As the seeds for epitaxial growth of shells, the highly loaded nanocrystals of SiO_2-Ag covered the interfaces of SiO_2 and are helpful to the epitaxial growth of shells in the process of synthesis TAP. **d**, The high-resolution TEM (HRTEM) image of nanocrystals on the core of SiO_2. Partial nanocrystals firmly embedded into the internal of amorphous SiO_2 core. The well-resolved interference fringe spacing of 0.24 nm corresponds to the interplanar distance between the (111) planes. **e**-**g**, HAADF-STEM images from low magnification to high magnification. The diameter of cores and the nanoceystals on the core are in range of 210-230 nm, and 5-25 nm, respectively. **h**-**k**, Energy dispersive X-ray (EDX) elemental mapping of (**h**). **l**, The area-normalized line-scanned elemental intensity profiles of (**h**). **m**, The Energy dispersive X-ray spectrometer (EDS) of the individual TAP of (**h**), the inset shows the details of element contents. **n**, The indicated lines corresponding to (**l**), the black line, green line, and the red line correspond to O, Si, and Ag, respectively.

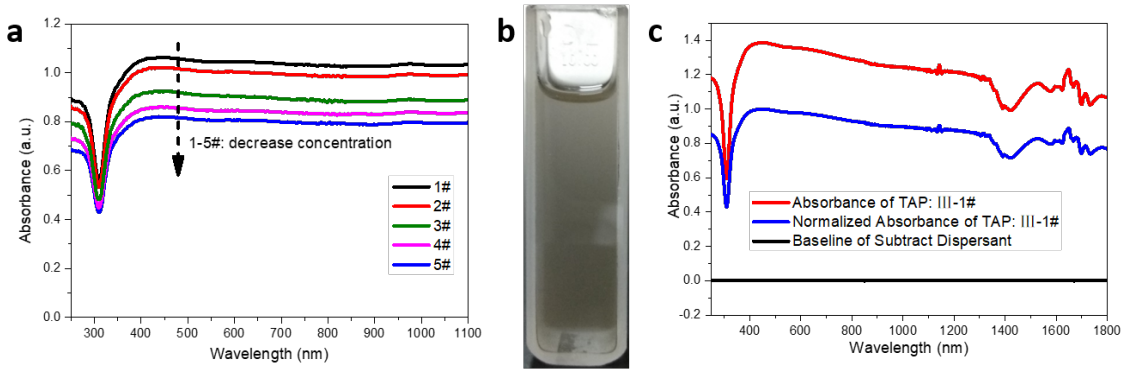

Figure 9. The profile of absorbance (a.u.) spectra of TAP maintains same profile and ultrabroadband coverage when gradually decline with the decreasing the concentration of TAP.

a, Optical property in terms of TAP (III-1#), the intensity of absorbance (a.u.) gradually decreases along with reducing its concentration, while the scope still maintains same profile and covers the same range, demonstrate that the optical spectra is corresponding to the individual TAP coupling enhanced plasmonic resonance absorbing spectrum. Each photoabsorber keeps relatively independent with each other duo to low concentration of TAP. **b**, The photo of TAP dilute colloid is light black in color corresponding to 3# in (**a**), the concentration of TAP in dilute colloid is so little that the colloid looks like transparent colorless. **c**, The strong, ultrabroadband and full-range plasmonic resonances absorbing spectra of TAP continuously full-range across the solar spectral irradiance (AM 1.5 Direct). Each TAP severs as the TAP of sunlight for full-range capturing sunlight, the strong and ultrabroadband plasmonic resonance absorbing spectrum (335-1800 nm) which covers 96.04% solar energy (AM1.5, 280-2500 nm). The baseline of subtract dispersant (black curve in (**c**)) fluctuates in the range of -0.0012 to 0.0016 a.u. which indicates the spectrophotometer is available to precisely measure the absorbance of TAP.

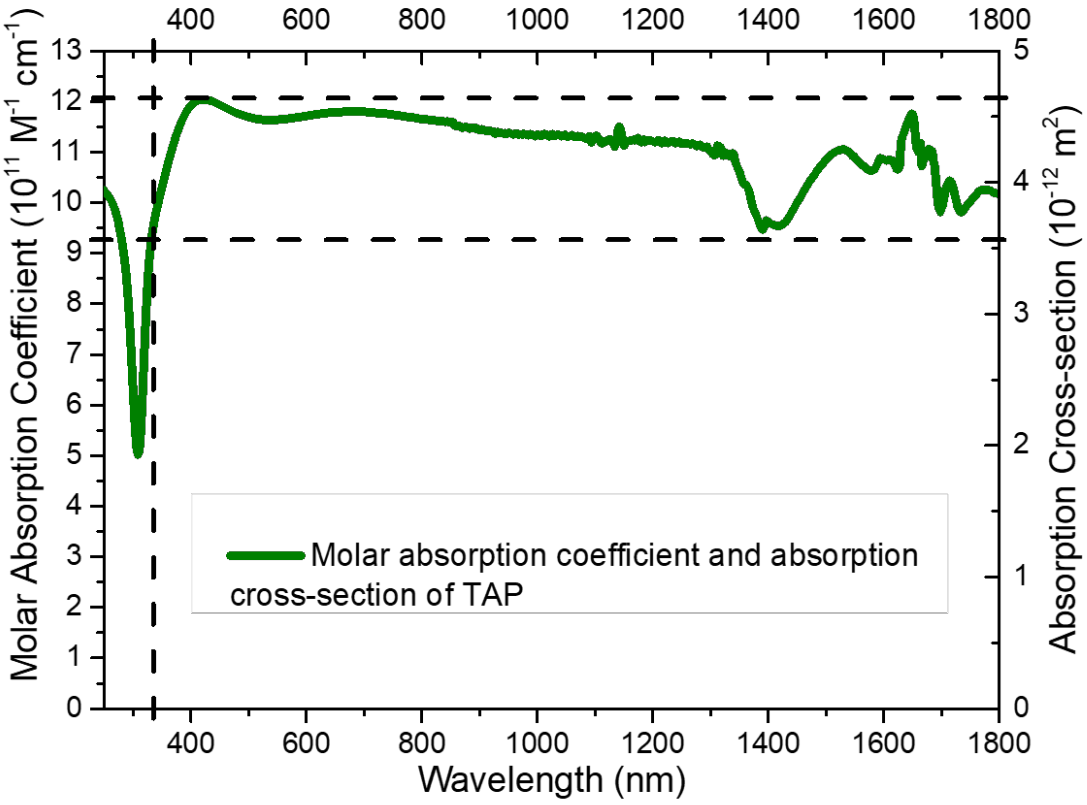

Figure 10. The absorption coefficient and the absorption cross-section of TAP (III-2#) with closed arranged bee-eyes shells.

Both the curve of molar absorption coefficient and the absorption cross-section of TAP along with the wavelength continually cover across the 335 to 1800 nm, which are totally different with the curve of molar absorption coefficient and the absorption cross-section of LSPR with finite and discontinuous absorbing peaks. The value of molar absorption coefficient and the absorption cross-section of TAP covering the range of 335-1800 nm is ~0.96-1.2 × 10^{12} M^{-1} cm^{-1} and ~3.6-4.6 × 10^{-12} m^2, respectively.

Table 1. The molar extinction/absorption coefficient (per mole of molecules or nanocrystals) of common photoabsorbers including molecular dyes, direct bandgap semiconductors, and based on LSPR photothermal nanomaterials.

Photoabsorber	Mechanism of capturing photon	Dimension (nm)	Molar extinction/absorption coefficient (M^{-1} cm^{-1})	Wavelength (nm)
Porfimer sodium[1]	Energy-level transition	Molecular	3×10^3	630
Benzoporphyrin derivative monoacid[1]	Energy-level transition	Molecular	3.5×10^4	689-693
Temoporfin[1]	Energy-level transition	Molecular	3×10^4	652
Motexafin lutetium[1]	Energy-level transition	Molecular	4.2×10^4	732
Sulfonated aluminium phthalocyanines[1]	Energy-level transition	Molecular	1.1×10^5	675
Zinc phthalocyanine[1]	Energy-level transition	Molecular	2.4×10^5	675
Tin etiopurpurin[1]	Energy-level transition	Molecular	2.8×10^4	660
Rhdamine 6G[2]	Energy-level transition	Molecular	1.2×10^5	530
Malachite Green[2]	Energy-level transition	Molecular	1.5×10^5	617
CdX (X = S, Se, Te)[2]	Bandgap absorption	r = 2	~$2\text{-}5 \times 10^5$	At excitonic maximum
CdTe nanocrystals[3]	Bandgap absorption	D: ~4-7 nm	~$2\text{-}6 \times 10^5$	~600-700
CdSe nanocrystals[3]	Bandgap absorption	D: ~1-7 nm	~$1\text{-}6 \times 10^5$	~300-700
CdS nanocrystals[3]	Bandgap absorption	D: ~1-6 nm	~$2\text{-}10 \times 10^5$	~250-450
Carbon nanotubes[2]	Energy-level transition (Van Hove Transitions)	r = 0.6, L = 150	7.9×10^6	808
Copper selenide[2]	Bandgap absorption	r = 8	7.9×10^7	970
Cu_9S_5 Nanocrystals[4]	Bandgap absorption	~70 nm ×13 nm	~1.2×10^9	980
Bimetal Sulphide[5]	Bandgap absorption	L = 149	5.68×10^{11}	915
Gold nanospheres[6]	LSPR	r = 20	7.7×10^9	530
Gold nanorods[7]	LSPR	R = 5, L = 27	1.9×10^9	650
Gold nanoshells[8]	LSPR	$r_1 = 55 \pm 5$, $r_2 = 65 \pm 5$	~2×10^{11}	820
TAP	CE-LSPR	r_1 = ~110, r_2 = ~135	**~$0.96\text{-}1.2 \times 10^{12}$**	**Coverage: 335-1800**

Note that the molar absorption coefficient of TAP continually covers across the 335 to 1800 nm (Figure S9), all the other photoabsorbers` molar absorption coefficient is corresponding to the peak wavelength with maximum of absorbance.

Table 2. The absorption cross-section (individual/single nanoparticle) of photoabsorber including noble metal nanostructures based on LSPR and TAP photothermal nanomaterials.

Photoabsorber	Shape and size (nm)	Mechanism of capturing photon	Cover/across spectrum (nm)	Absorption cross-section (m^2)
Ag octahedrons[9]	R = 23	LSPR	455 ± 55	6.8×10^{-15}
Au nanoparticles[10]	D = 88	LSPR	580 ± 50	2.2×10^{-14}
Au nanorod[11]	D = 6.0 ± 0.6, L = 16.3 ± 3.7	LSPR	726 ± 66	2.4×10^{-16}
Au nanorod[11]	D = 8.8 ± 0.6, L = 36.6 ± 4.0	LSPR	726 ± 85	1.4×10^{-15}
Au naorod[11]	D = 40.2 ± 2.8, L = 104.3 ± 7.0	LSPR	727	1.2×10^{-14}
Au nanorod[11]	D = 16.6 ± 1.3, L = 66.2 ± 5.4	LSPR	808	6.6×10^{-15}
Au nanorod[12]	D = 20 nm, L = 60 nm	LSPR	780 ± 30	2.3×10^{-14}
Au rod-in-shell[12]	D = 20 nm, L = 60 nm, T = 4 nm, G = 5 nm	LSPR	690 ± 30, 1180 ± 50	3.0×10^{-14}, 2.0×10^{-14}
Gold nanobar[13]	L=320	LSPR	1740 ± 100	1.93×10^{-14}
Gold nanobar[13]	L = 440	LSPR	2200 ± 100	3.15×10^{-14}
Gold contour nanobar[13]	L = 255	LSPR	1730 ± 100	2.13×10^{-14}
Gold contour nanobar[13]	L = 360	LSPR	2210 ± 100	3.39×10^{-14}
Gold nanodisk chain[13]	L = 240	LSPR	1740 ± 100	1.48×10^{-14}
Gold nanodisk chain[13]	L = 352	LSPR	2200 ± 100	3.08×10^{-14}
Gold nanoring chain[13]	L = 192	LSPR	1780 ± 100	8.5×10^{-14}
Gold nanoring chain[13]	L = 256	LSPR	2230 ± 100	1.51×10^{-14}
Hollow gold nanoshells[14]	L = 20-38	LSPR	650-850	1.1×10^{-14}
metallo-dielectric nanomatryoshkas[15]	r_1 = 21, r_2 = 30, r_3 = 45	LSPR	~780 ± 30	3.0×10^{-14}
metallo-dielectric nanoshells[15]	r_1 = 60, r_2 = 73, r_3 = 75	LSPR	~620 ± 30	3.8×10^{-14}
Gold–Silica Nanoshells[8]	D = 110 ± 11 nm, 10 nm-thick gold shell	LSPR	820 ± 100	3.8×10^{-14}
SiO_2/Au Nanoshells[16]	r_1 = 60, r_2 = ~70	LSPR	800 ± 150	$\sim 8.5 \times 10^{-14}$
Ag/Au core/shell[17]	5 nm shell thickness	LSPR	600-900	1.8×10^{-13}
Silica–Au core–shell[18]	r_1 = 94 ± 9 nm, thickness: 9, 15, 21, 27,33 nm	LSPR	700-1000	4×10^{-13}
TAP	**nanoshells, r_1 = ~110, r_2 = ~160**	**CE-LSPR**	**Coverage: 335-1800**	**~3.6-4.6 × 10^{-12}**

Note that the absorption cross-section of TAP continually full-range absorbing spectrum covers across the 335 to 1800 nm (Figure S9) rather than the finite and discontinuous absorbing peaks of LSPR, all the other photoabsorbers` absorption cross-section is corresponding to the peak wavelength with maximum of absorbance.

Table 3. The tunable absorbance (a.u.) spectra of noble metal nanostructures based on LSPR and TAP photothermal nanomaterials.

Shape of photoabsorber	Tunable range of plasmon resonance absorbing spectra (nm)	Profile of peak of spectra	Mechanism of capturing photon	Reference
Ag nanosphere and quasi-nanosphere	320-450	Discontinuous one absorbing peak	LSPR	[19]
Ag nanocube and truncated nanocube	400-480	Discontinuous one absorbing peak	LSPR	[19]
Ag nanotetrahedron and truncated nanotetrahedron	350-450, 642-673	Discontinuous two absorbing peaks	LSPR	[19]
Ag nanooctahedron and truncated nanooctahedron	400-500	Single absorbing peak	LSPR	[19]
Ag nanobar	350-900	Discontinuous two absorbing peaks	LSPR	[19]
Ag nanospheroid	350-900	Discontinuous two absorbing peaks	LSPR	[19]
Ag right nanobipyramid	500-700	Discontinuous three absorbing peaks	LSPR	[19]
Ag nanodecahedron	350-450	Discontinuous two absorbing peaks	LSPR	[19]
Ag nanowire and nanorod	380-460	Discontinuous two absorbing peaks	LSPR	[19]
Ag nanoprisms	340, 450-750	Discontinuous two absorbing peaks	LPPR	[20]
Ag nanoplate and nanodisc	350-1000	Discontinuous multiple absorbing peaks	LSPR	[19]
Ag branched nanostructures	400-1000	Discontinuous multiple absorbing peaks	LSPR	[19]
Ag hollow nanostructures	380-800	Discontinuous multiple absorbing peaks	LSPR	[19]
Ag nanoparticles	400-715	Discontinuous one or two absorbing peaks	LSPR	[21]
Ag nanocages	370-810	Discontinuous two absorbing peaks	LSPR	[22]
Gold Nanoparticles	517-575	Discontinuous one absorbing peak	LSPR	[23]
gold nanoaggregates	522-620	Discontinuous two absorbing peaks	LSPR	[24]
Au nanorods	650-1050	Discontinuous two absorbing peaks	LSPR	[25]
Gold Nanorods	520-950	Discontinuous two absorbing peaks	LSPR	[26]
Au nanocages	450-900	Discontinuous one absorbing peak	LSPR	[27]
Au nanostars	630-950	Discontinuous two absorbing peaks	LSPR	[28]
Au nanoflowers	548-628	Discontinuous two absorbing peaks	LSPR	[29]

Gold bellflower	600-820	Discontinuous one absorbing peak	LSPR	[30]
Gold nanoparticle-hydrogel composites	550-570	Discontinuous one absorbing peak	LSPR	[31]
Plasmonic vesicles	531	Discontinuous one absorbing peak	LSPR	[32]
Hollow Au-Ag nanoshells	660-800	Discontinuous one broadened absorbing peak	LSPR	[33]
Hollow Gold−Silver Nanospheres	~630-850	Discontinuous one absorbing peak	LSPR	[34]
Hollow AgAu NPs	535-575	Discontinuous one absorbing peak	LSPR	[35]
Pd@Au nanocages	540-785	Discontinuous one absorbing peak	LSPR	[36]
Ag_{core}-Au_{shell} bimetallic nanoparticles	402-508	Discontinuous two absorbing peaks	LSPR	[37]
Gold–silver nanoparticles	400-530	Discontinuous one absorbing peak	LSPR	[38]
$Ag_{core}Au_{shell}$ nanoparticles	~420-580	Discontinuous one or two absorbing peaks	LSPR	[39]
Gold−Silver nanoshells	~500-900	Discontinuous one broadened absorbing peak	LSPR	[40]
Au@Ag NRs	347, 390, 537	Discontinuous three absorbing peak	LSPR	[41]
Au–Ag nanocages	450-760	Discontinuous one absorbing peak	LSPR	[42]
Gold-silver nanocages	434-870	Discontinuous multiple broadened absorbing peaks	LSPR	[43]
Au−Ag hybrid NSs	800-1100	Discontinuous multiple absorbing peaks	LSPR	[44]
Gold-coated Au_2S Nanoshells	600-100	Discontinuous two absorbing peaks	LSPR	[45]
Hollow gold nanospheres	550-830	Discontinuous one absorbing peak	LSPR	[46]
Hollow gold nanoshells	650-900	Discontinuous one absorbing peak	LSPR	[47]
Hollow gold nanospheres	640-710	Discontinuous one absorbing peak	LSPR	[48]
Gold shell/polystyrene core	514-875	Discontinuous two absorbing peaks	LSPR	[49]
Porous silica-coated hollow gold−silver nanoshells	~445-800	Discontinuous one broadened absorbing peak	LSPR	[50]
Au@SiO_2 Nanoparticle/PDADMAC multilayers	588-642	Discontinuous one broadened absorbing peak	LSPR	[51]
Ag/Au core/shell	600-900	Discontinuous two broadened absorbing peaks	LSPR	[17]
Gold-palladium alloy nanoshell	~780	Discontinuous one broadened absorbing peak	LSPR	[52]
Silica core gold shell	~620-900	Discontinuous one absorbing peak	LSPR	[53]

Silica–Au core–shell	~700-1000	Discontinuous one absorbing peak	LSPR	[18]
SiO_2−Au core−shell nanoparticles	689-741	Discontinuous two absorbing peaks	LSPR	[54]
Bimetallic hollow Au-Ag nanoshells	438-937	Discontinuous one absorbing peak	LSPR	[55]
RF-core@Ag-shell	400-900	Discontinuous one broadened absorbing peak	LSPR	[56]
PSA@Ag-NPs	450-500	Discontinuous one broadened absorbing peak	LSPR	[57]
Glutathione-capped AuNP clusters	520-550	Discontinuous one broadened absorbing peak	LSPR	[58]
silica–Au core–shell nanoparticles	700-100	Discontinuous one broadened absorbing peak	LSPR	[59]
Goldsilicagold multilayer Nanoshells	600-1100	Discontinuous multiple absorbing peaks	LSPR	[60]
Au/SiO2/Au nanoparticles	600-950	Discontinuous multiple absorbing peaks	Fano resonances	[61]
Self-assembled plasmonic nanoparticle clusters	650-1450	Discontinuous multiple absorbing peaks	Fano-like resonance	[62]
Ag@SiO_2@AgNPs	500-550	Discontinuous one broadened absorbing peak	LSPR	[63]
Ag satellite NPs	533-677	Discontinuous one or two absorbing peaks	LSPR	[64]
Silica-coated gold nanoflowers	600-625	Discontinuous one absorbing peak	LSPR	[65]
Core (SiO_2)−satellite (Ag) nanoclusters	~350, 480	Discontinuous two broadened absorbing peaks	LSPR	[66]
Branched nanoporous gold Nanoshells	750-850	Discontinuous one broadened absorbing peak	LSPR	[67]
Gold dimers	572-855	Discontinuous multiple absorbing peaks	Quantum plasmonic dimer antennas	[68]
Nanoshell dimers	600-930	Discontinuous two absorbing peaks	LSPR	[69]
Au rod-in-shell	600-1300	Discontinuous multiple absorbing peaks	LSPR	[70]
Superparamagnetic gold Nanoshells	520~-900	Discontinuous one broadened absorbing peak	LSPR	[71]
Amphiphilic plasmonic micelle-like nanoparticles	530-743	Discontinuous two absorbing peaks	LSPR	[72]
TAP	**Coverage: 335-1800**	**Continually full-range absorbing spectrum**	**CE-LSPR**	This work

Note that the tunable absorbing spectra are different with the coverage absorbing spectra, the discontinuous one or multiple absorbing peaks of absorbance spectrum involving to LSPR absorbers is available to be tuned across a broad region of spectrum in the range of UV-vis-NIR, thus the wide tunable spectral range do not mean the wide coverage absorbing spectra.

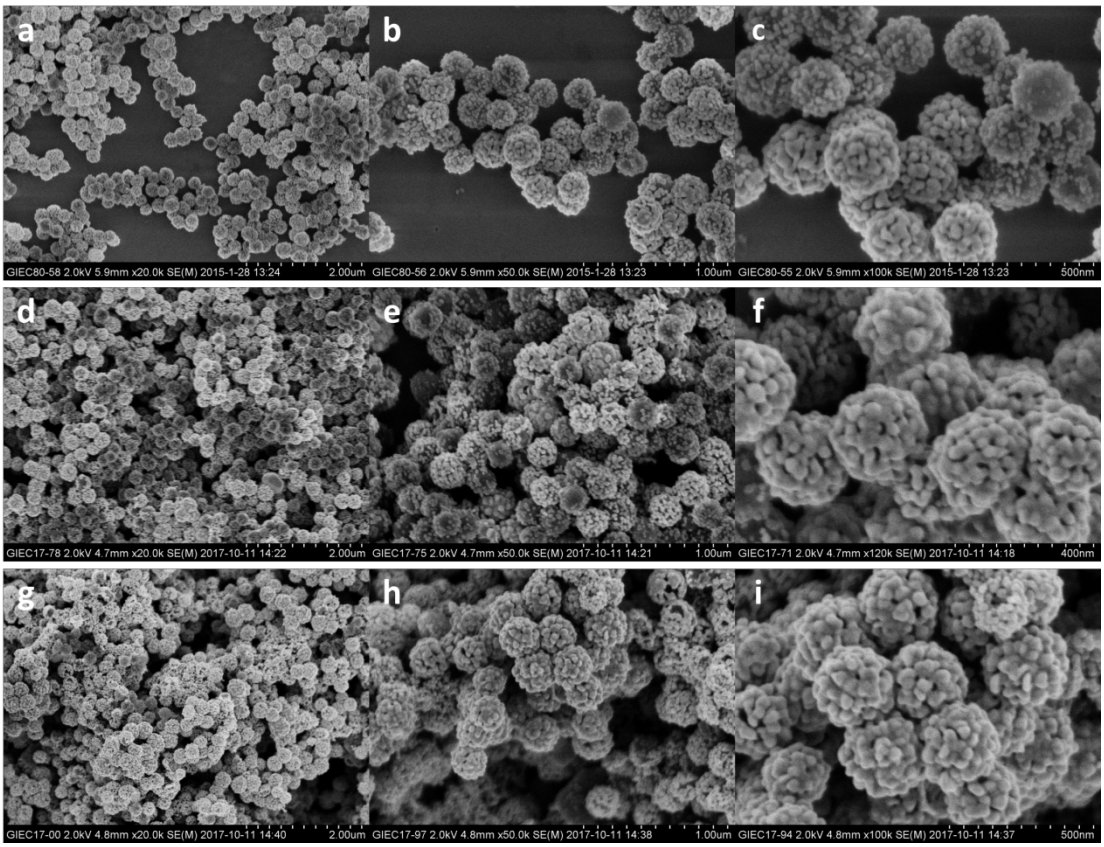

Figure 11. The closed arranged bee-eyes shells of TAP (III-1#) and extreme stability.

a-c, The SEM image of initial TAP ranging from low magnification to high magnification. **d-f**, The SEM image of long-term stored TAP ranging from low magnification to high magnification. The shelf-life duration was more than 33 months. **g-i**, The SEM image of TAP which employed to generate solar steam ranging from low magnification to high magnification. It demonstrates that the sort of TAP is available to generate high temperature ($>$ 105 ℃) solar steam thanks to its extreme stability.

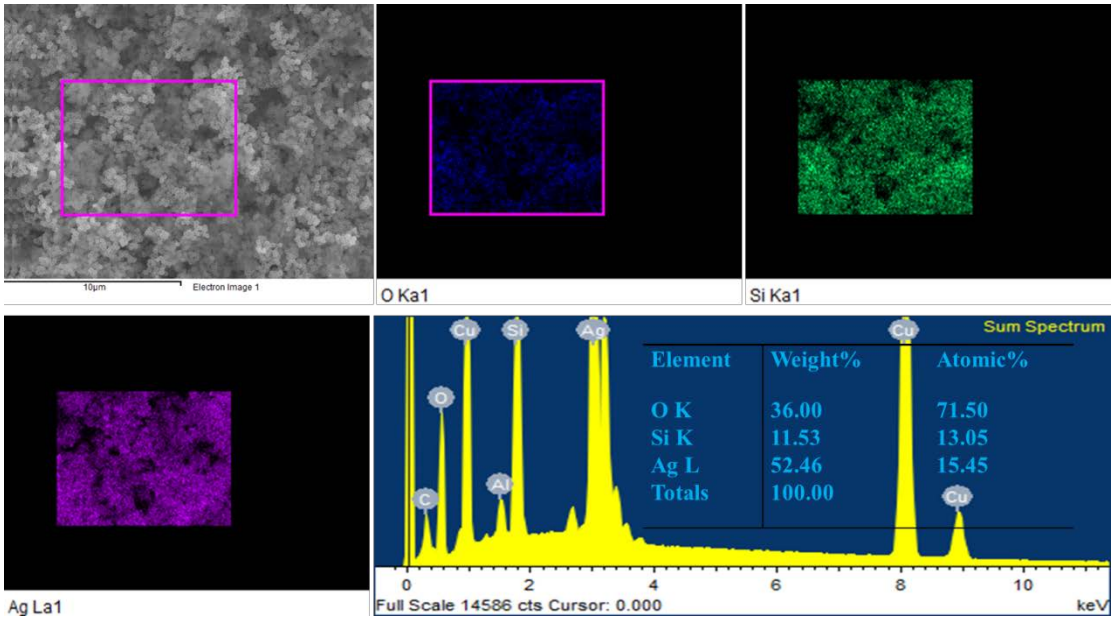

Figure 12. The SEM-EDS images of extreme stability and highly covered and closed arranged bee-eyes shells in terms of TAP (III-1#).

The measured TAP dispersion had been stored under ambient condition more than 33 months before employed EDS measurement.

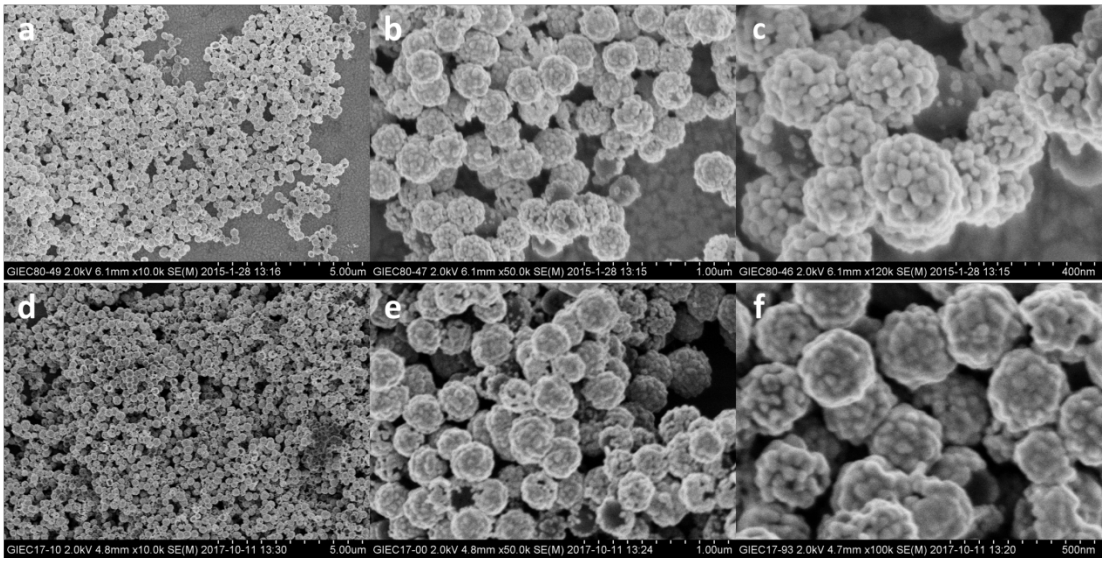

Figure 13. The closed arranged bee-eyes shells of TAP (III-2#) and extreme stability.

a-c, The SEM image of initial TAP ranging from low magnification to high magnification. **d-f**, The SEM image of long-term stored TAP ranging from low magnification to high magnification. The shelf-life duration was more than 33 months.

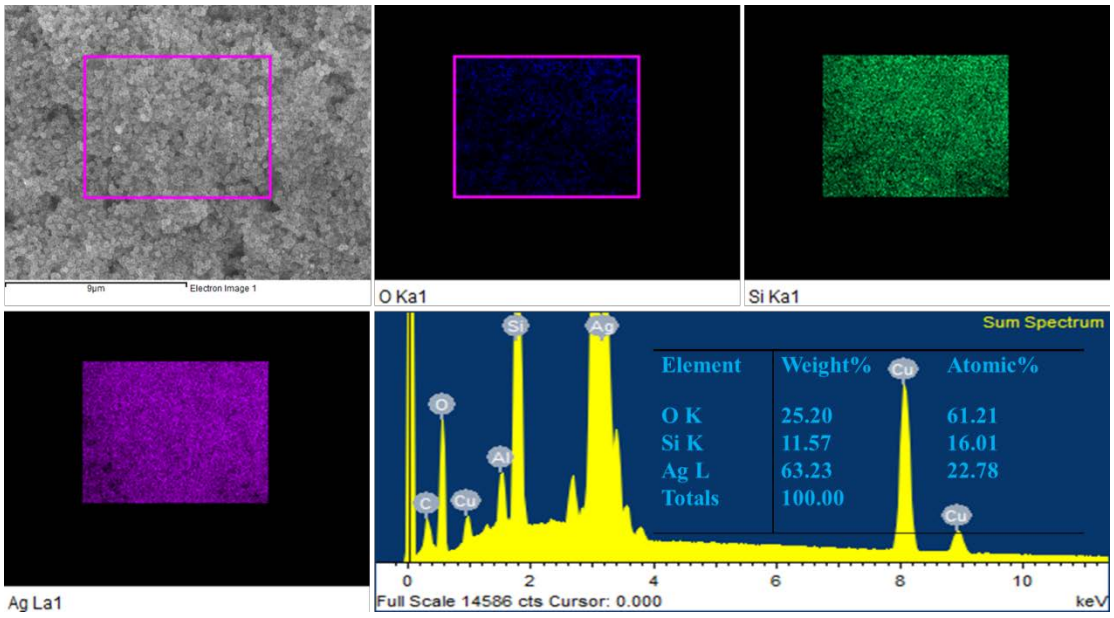

Figure 14. The SEM-EDS images of extreme stability and highly covered and closed arranged bee-eyes shells in terms of TAP (III-2#).

The measured TAP dispersion had been stored under ambient condition more than 33 months before employed EDS measurement.

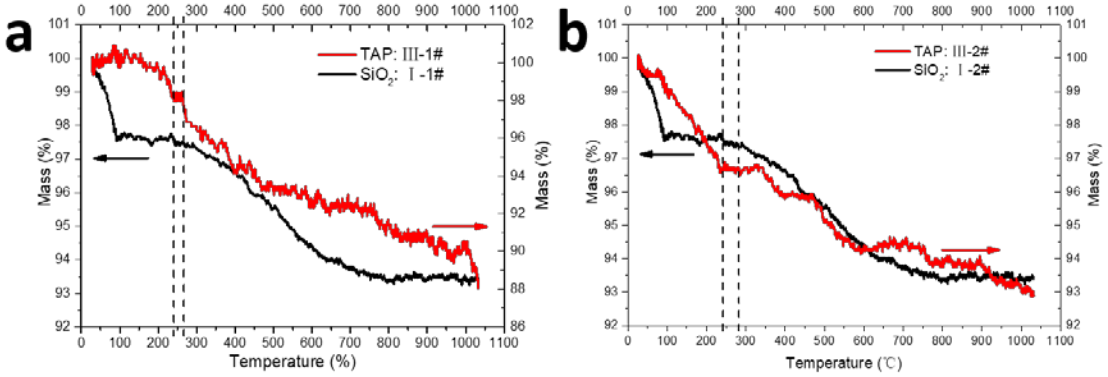

Figure 15. The thermogravimetry (TG) curves of TAP.

a, The TG curves include SiO_2 (I-1#) and TAP (III-1#). **b**, The TG curves include SiO_2 (I-2#) and TAP (III-2#). TG testes revealed the melting temperature of shells of TAP (III-1#) ranging from 238.7 ℃ to 265.1 ℃, another sample of TAP (III-2#) would melt in the range of 236.1-281.9 ℃. TG was measured by a STA 409 PC (NETZSCH) with a heating rate of 10 ℃/min in flowing argon 60 ml/min.

Text 1. The extreme stability of TAP

As a prerequisite for the heat source via the powerful hot-spots, the stability of TAP is essential for evaporating the surrounding bulk medium to generate high temperature steam. As for TAP, the mechanism of extreme stability includes thermodynamics of composite nanoshells and the crystallographic configuration. The case of TAP in the way of closed arranged bee-eyes shells is particularly conducive to improve the stability of shell, since the most interfaces/surfaces of Ag nanoparticles combine with each other and the internal surfaces also combine with the core surface, only ever a small fraction of surfaces being exterior surfaces of shells (outshells) is exposed. The total potential energy of the shells is minimized as far as possible leading to vastly improves the stability, while maintains its activity of the exterior surface. The dispersion of SiO_2-Ag (II-1#) was safely stored more than 33 months in ambient temperature (Figure S3-S5, Supporting Information), without morphologic damage or component change, as well as the sample SiO_2-Ag (II-2#) showed long-term stability (Figure S7,S8, Supporting Information). The dispersion of TAP also showed well extreme stability (Figure 1-2 and Figure S11-S14, Supporting Information) when stored more than 33 months under ambient condition. TAP also maintain their morphology after employed to generate solar steam (Figure S11g-i, Supporting Information).

On the subject of the crystallographic configuration stability, according to quantitative analysis in XRD patterns, the intensity ratio between (200) and (111) diffraction peaks of TAP (III-1#, III-2#) (Figure S1d,h, Supporting Information) is 0.190 and 0.136, respectively, both are lower than the classic value of silver crystal (0.45)[74], and so is the ratio of intensity between (220) and (111) peaks (0.090 (III-1#), 0.108 (III-2#) versus 0.25). It verifies that the subsequent epitaxial growth of closed arranged bee-eyes shells is strongly inclined to be enclosed by the low-index crystalline planes with close atomic packing and extreme stability (Figure1d, Figure 2d, and Figure S1d,h, Supporting Information). The TAP is spontaneously abundant in the most stable (111) plane of fcc silver shells which is great beneficial for stability. The term of melting temperature is important parameter for the photothermal conversion procedure. The thermogravimetry (TG) tests reveal the melting temperature of shell of TAP (III-1#) ranging from 238.7 to 265.1 ℃ (Figure S15a, Supporting Information), another sample of TAP (III-2#) would melt in the range of 236.1-281.9 ℃ (Figure S15b, Supporting Information). Although, the thickness of the shell is less than 60 nm, both the melting temperature of them are higher than the Ag nanoparticles (melting temperature: ~180 ℃) with diameter 118 ± 31 nm[75]. The comparison further confirms the extreme stability of TAP. Since the macroscopic temperature of TAP is more than 600 ℃, it is supposed to generate high temperature steam, the steam temperature is possible to up to 236 ℃ using TAP for harvesting solar energy.

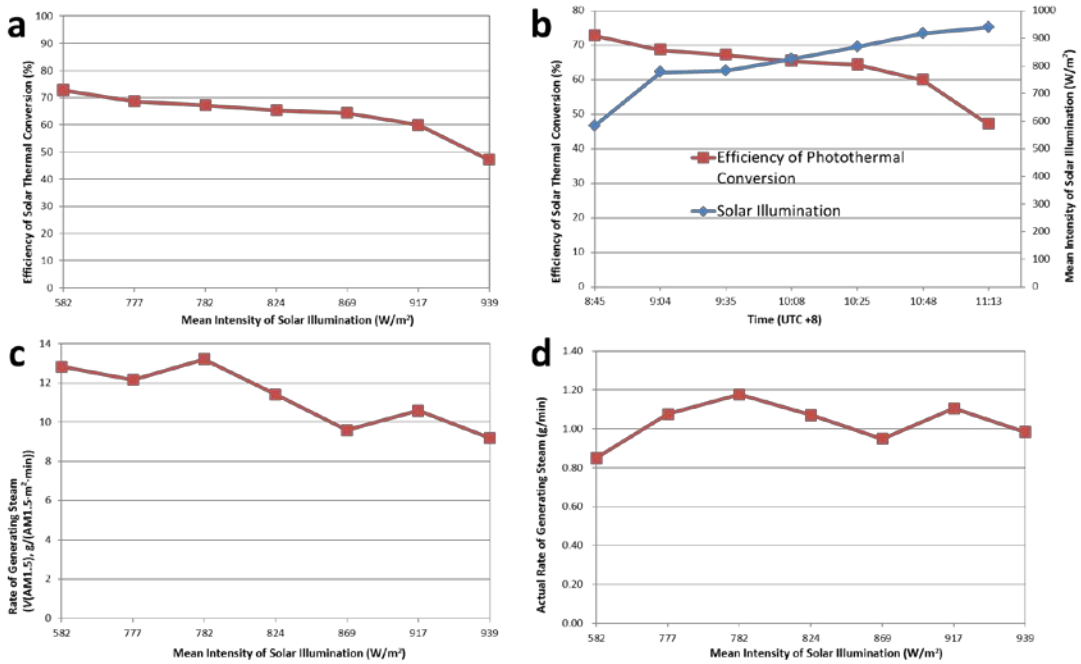

Figure 16. The overall performances of solar steam driven by TAP involved concentration of Section I.

a, The curve of η_{ce} along with varying the intensity of natural sunlight in outdoor tests. **b**, The curves of η_{ce} and intensity of natural sunlight correspond to the local time. The contrast of curve trend illustrates that the sort of TAP employing low-level efficient η_c in daytime (08:45 am to 11:13 am), particularly in under high intensity of natural sunlight (824-939 W/m^2), because that the concentration of TAP is not sufficient to capture incident sunlight. **c**,**d**, The curve of V(AM1.5) and V_a along with varying the intensity of natural sunlight in outdoor tests. In each outdoor test, the low concentration of TAP (III-1#) was ~7 × 10^{12} photoabsorbers/L, harvesting irradiation area: 35 × 35 cm.

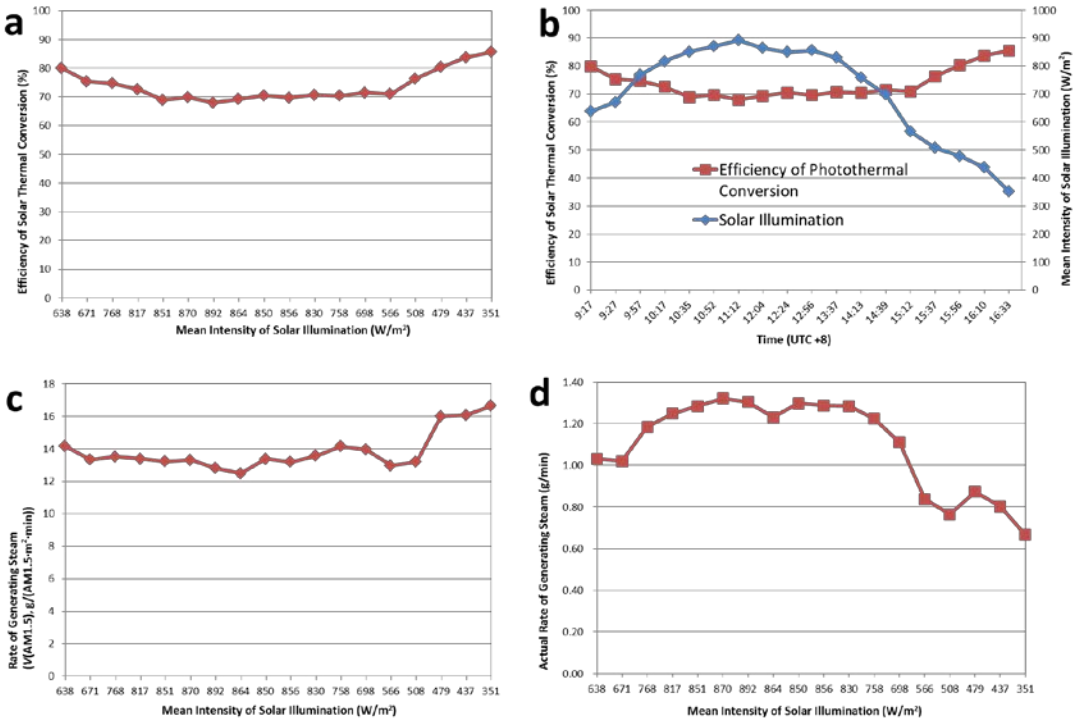

Figure 17. The overall performances of solar steam driven by TAP involved relative low concentration of Section II.

a, The curve of η_{ce} along with varying the intensity of natural sunlight in outdoor tests. **b**, The curves of η_{ce} and intensity of natural sunlight correspond to the local time. The contrast of curve trend illustrates that the sort of TAP employing excellent η_c in full daytime (09:17 am to 16:33 pm), particularly in under weak intensity of natural sunlight (351-508 W/m^2). **c**,**d**, The curve of V(AM1.5) and V_a along with varying the intensity of natural sunlight in outdoor tests. The overall performances of solar steam on the Section II has been great improved, while still have room for better overall performances. In each outdoor test, the relative low concentration of TAP (III-1#) was ~1.2 × 10^{13} photoabsorbers/L, harvesting irradiation area: 35 × 35 cm.

Table 4. The experimental details of parameters in terms of Section IV, and the performances in terms of generation steam by TAP (sample III-1#).

NO.	a	b	c	d	e	f	g	h	i	j	k	l
1	34.09	30.13	3.96	29-48	875	180	10204.1	2404.4	17943.2	70.27	13.24	1.32
2	33.94	29.38	4.56	33-50	910	180	11673.6	2097.7	18660.9	73.80	14.66	1.52
3	32.42	26.21	6.21	42-65	719	296	15662.9	2531.9	24246.0	75.04	15.37	1.26
4	33.43	27.36	6.07	48-60	690	240	15156.8	1379.9	18866.0	87.65	19.30	1.52

a: Initial weight of TAP (III-1#) dispersed in DI water (g); b: Terminal weight of AgNPs dispersed in DI water (g); c: Steam (m); d:Temperature change (℃); e: Mean power density of solar energy (W/m^2); f: Irradiation time (s); g: Absorption energy of steam (J); h: Absorption energy of solution; i: Irradiation energy; j: Solar thermal conversion efficiency (η_{ce}) (%); k: Rate of steam (V(AM1.5), $g/(AM1.5 \cdot min \cdot m^2)$); l: the actual rate of steam (V_a, g/min).

Text 2. The performances analysis of solar thermal conversion drives by TAP to efficiently generate high temperature steam with high rate

We analyze the solar thermal conversion performances of the case of 4# in Table S1 which corresponds to last case in main text Figure 5a. The TAP (III-1#) was irradiated under natural solar irradiation with the average 690 W/m^2, typically, the initial weigh of the dispersion is 33.43 g consisting about 1.3 × 10^{15} photoabsorbers/L TAP (III-1#)，after both vigorously stirring and ultrasonic dispersion 3-5 mins, straightforward illuminated by focused sunlight. After the initial period which debugged the angle and the distance of Fresnel lens to focus the sunlight on the dispersion, and response time of superheated steam. As for the stable and continuous incident illumination, steady-state system, the rate of evaporating steam via TAP absorption approximately linear along with the irradiation time, corresponding to the mass loss curve in main text Figure 5e (blue line corresponding 690 W/m^2 in Figure 5d). The mass loss in term of steam is 6.07 g, t = 4 mins, the solution temperature increases from 48 to 60 ℃. Both the latent heat of vaporization and heat capacity are slightly depend on the transient temperature, and the extent of variation is far less its value, herein, to simplify the calculation procedure, we deem them as constants, latent heat of vaporization and heat capacity are 2257.6 kJ/kg, and 4.2 kJ/(kg·K), respectively. According to the temperature curve in Figure S18,S19 and main text Figure S23, the superheated steam/vapor temperature is above 105 ℃, so the energy of localized steam generating 6.07 g in 4 mins is 15156.79 J, and the solution increasing temperature needs 1378.94 J. The capturing solar energy via Fresnel lens with an area with 35 × 35 cm and sunlight transmittance 88% - 93%, the intensity of solar irradiation was 686-694 W/m^2, using the mean 690 W/m^2 and sunlight transmittance 93% for calculation, is 18865.98 J. So the solar thermal conversion efficiency is 87.65%, corresponding the rate of steam (V(AM1.5)) and the actual rate of steam are 19.30 g/(AM1.5·m^2·min) and 1.52 g/min ,respectively.

The background test of DI water volatilization under sunlight irradiation, the same capacity beaker being filled up with DI water, about 38 ml DI water and the weight of DI water was 38.34g, the intensity of solar irradiation was 755-871 W/m^2, the surrounding temperature 24-26 ℃, relative humidity (RH) more than 50%, after volatilizing 1 h (10:08 a.m. to 11:08 a.m.), the volatilization is 0.82 g, and the volatilization rate is average 0.0137 g/min. All the cases, the mass loss of DI water attributing to volatilization has been deducted to measure the overall performances of solar steam generation only from TAP.

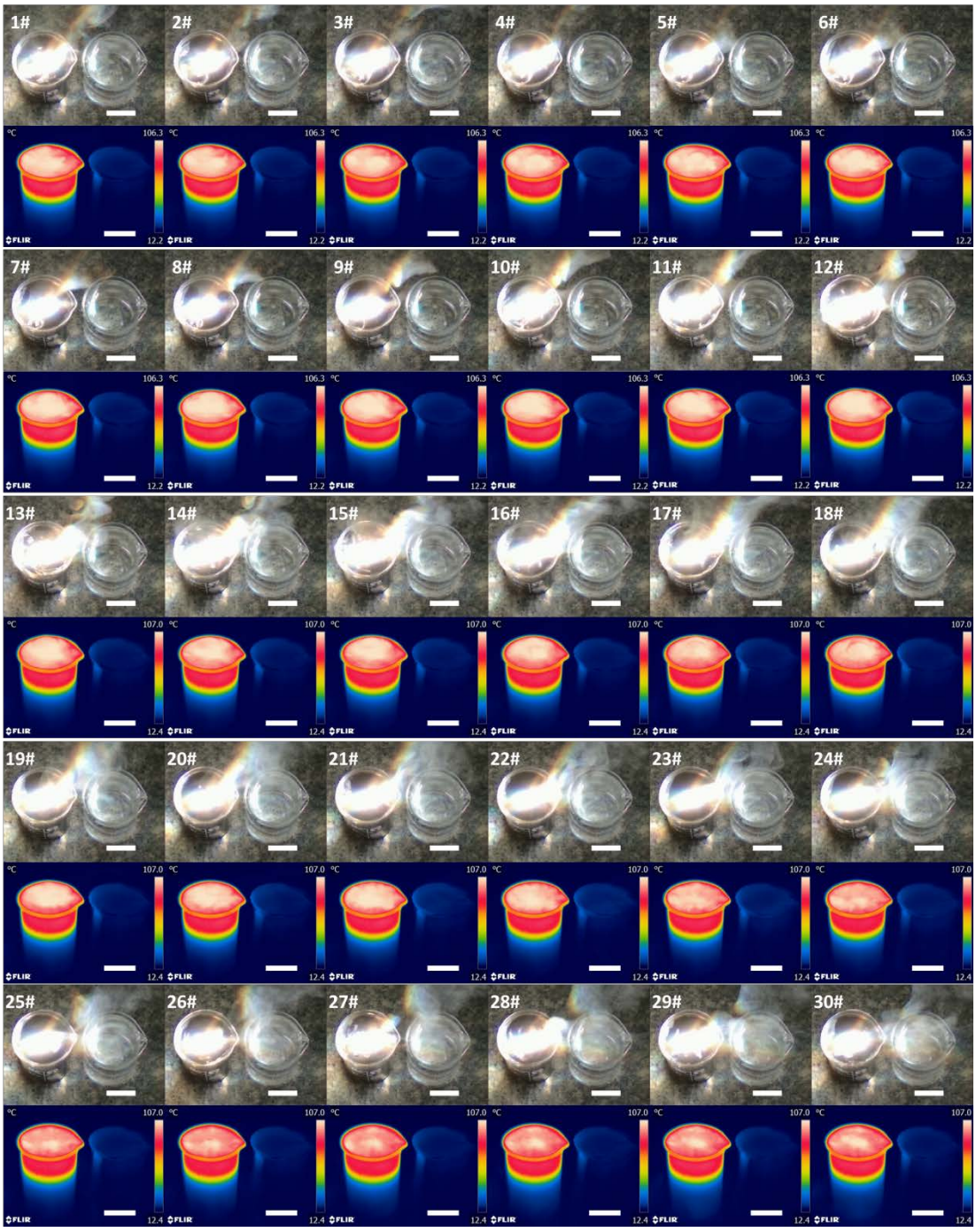

Figure 18. The in-site captures of continuously produce drastic boiling steam in 1 s driven by TAP involved higher concentration of Section IV.

1-30#, The instant capture of generating vast solar steam, it obviously shows the instant situation of vast steam rapidly released only in the irradiating area involving the interface of liquid-air, as well as the bubbles mingled with explosive whistle. The thermal infrared imaging recorded by IR camera below (1-30#) corresponding the temperature distribution shows the huge temperature gradient (> 90 ℃) and the high temperature of localized solar steam (> 105 ℃). In each outdoor test, the concentration of TAP (III-1#) was ~2.4 × 10^{13} photoabsorbers/L, harvesting irradiation area: 35 × 35 cm. In each case, the scale bar is equal to 2 cm.

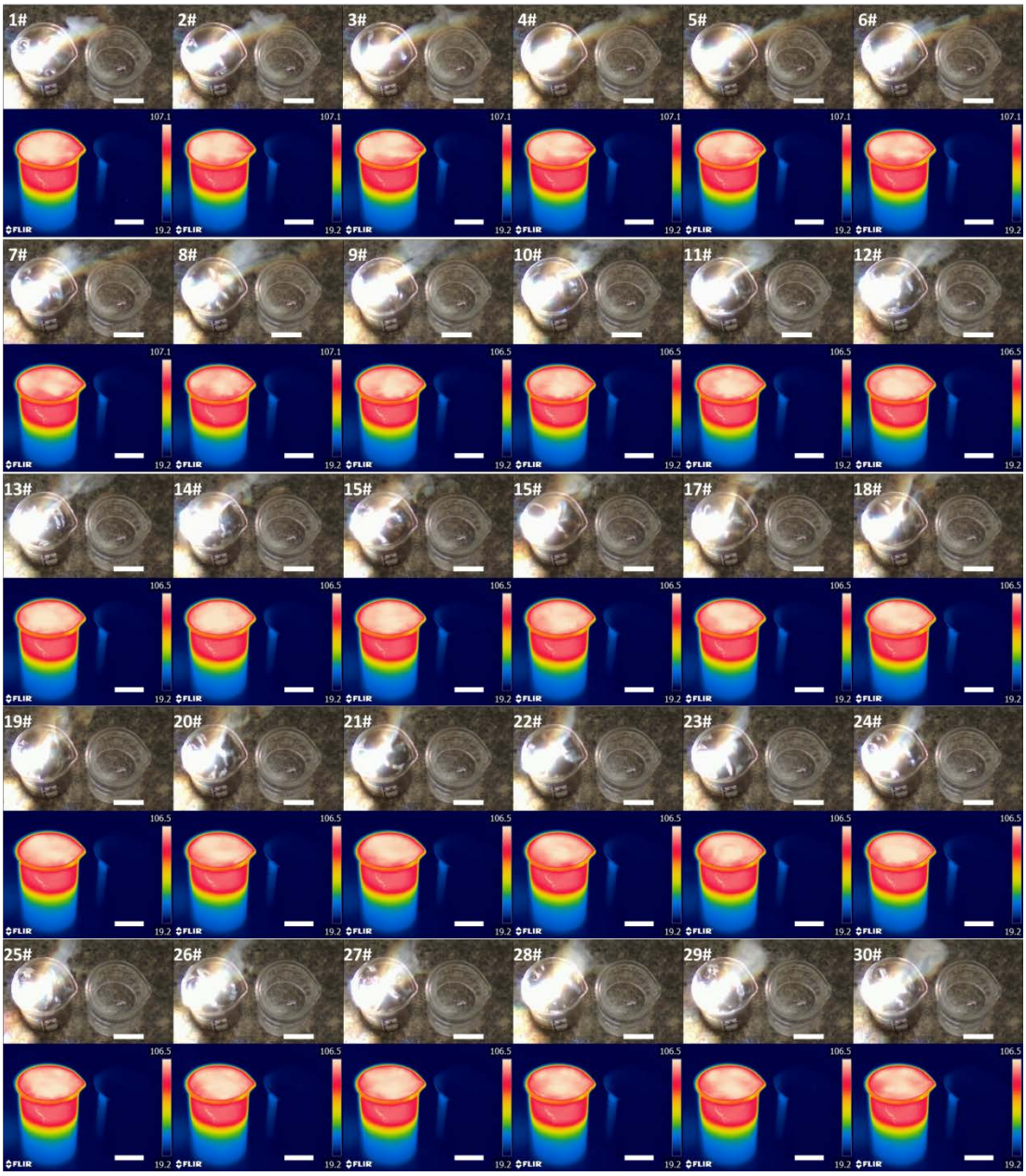

Figure 19. The in-site captures of continuously produce drastic boiling steam in 1 s driven by TAP involved proper concentration of TAP (III-2#).

1-30#, The instant capture of generating vast solar steam obviously shows the instant situation of vast steam rapidly released only in the irradiating area involving the interface of liquid-air, as well as the bubbles mingled with explosive whistle. The thermal infrared imaging recorded by IR camera below (1-30#) corresponding the temperature distribution shows the huge temperature gradient (＞ 85 ℃) and the high temperature of localized solar steam (＞ 105 ℃). In each outdoor test, the concentration of TAP (III-2#) was ~2 × 10^{13} photoabsorbers/L, harvesting irradiation area: 35 × 35 cm. In each case, the scale bar is equal to 2 cm.

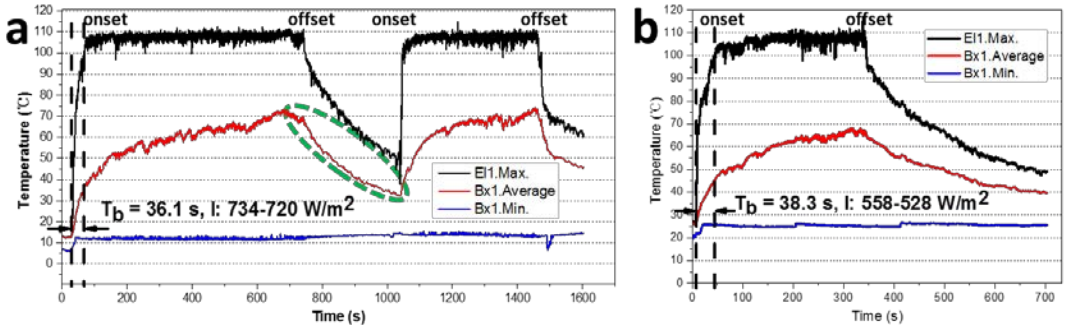

Figure 20. The temperature curves in the process of produce solar steam driven by TAP and the cooling rate involved low concentration of Section I.

a,**b**, The temperature curves in the whole process of generating solar steam via low concentration TAP (~7 × 10^{12} photoabsorbers/L) show slow response time of boiling vapor (T_b) varying the intensity of sunlight at given low concentration of TAP. The dotted ellipse with green color marked in (**a**) corresponds to the cooling stage.

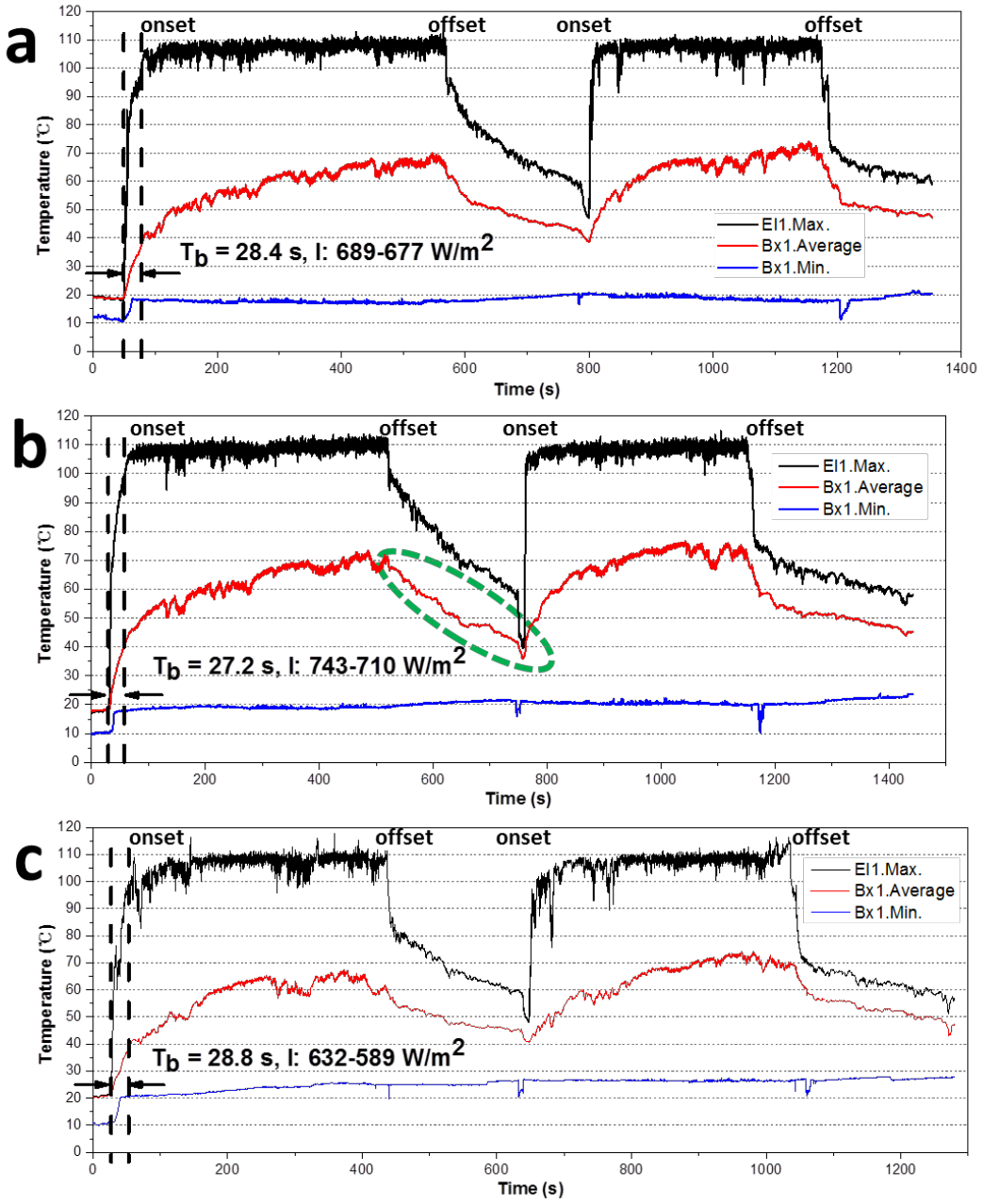

Figure 21. The temperature curves in the process of produce solar steam driven by TAP and the cooling rate involved low concentration of Section II.

a-c, The temperature curves in the whole process of generating solar steam via relative low concentration TAP (~1.2 × 10^{13} photoabsorbers/L) show relative slow response time of boiling vapor (T_b) varying the intensity of sunlight at given low concentration of TAP. The dotted ellipse with green color marked in (**b**) corresponds to the cooling stage.

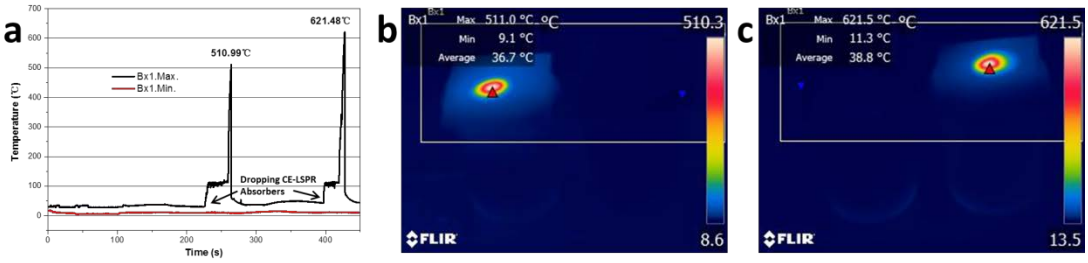

Figure 22. The macroscopic temperature of hot-spots of stacking TAP under irradiation of focused sunlight.

a, The temperature curves of the box measurement include the maximum value (Bx1.Max.) and the minimum value (Bx1. Min.) which represent the maximum temperature of irradiating area (black line) and the ambient temperature (red line), respectively. **b**, The capture of IR image shows the macroscopic temperature of hot-spots in the first test of (a). As the first test, dropwise added 20 droplets (~1 ml) suspension of TAP obtained the macroscopic temperature of hot-spots of stacking TAP 510.99 ℃ corresponding the first peak of black line in (a). **c**, The capture of IR image shows the macroscopic temperature of hot-spots in the second test of (a). As the second test, dropwise added 27 droplets (~1.35 ml) suspension of TAP, the macroscopic temperature of hot-spots of stacking TAP was up to 621.48 ℃ corresponding the second peak of black line in (a). The intensity of sunlight ranged from 701 to 776 W/m^2, the whole course is shown in Supplementary Video 1. The above test demonstrated that the macroscopic temperature of hot-spots of stacking TAP was relative to the concentration of photoabsorber at given irradiation and the same sort photoabsorber.

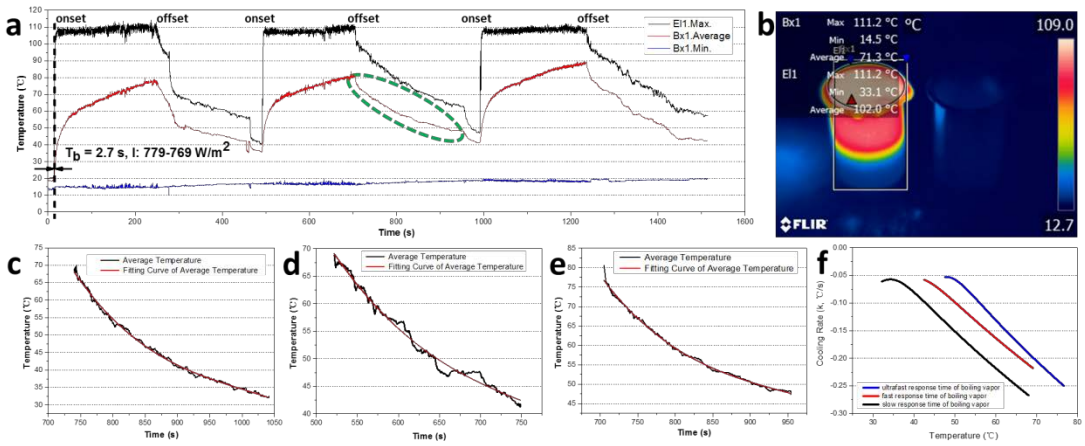

Figure 23. The temperature curve in the process of generating solar steam driven by TAP and the cooling rate.

a, The temperature curves of generating solar steam via TAP include the maximum of temperature Ellipse measurement (El1.Max.) locating in liquid-air interface, the average of temperature Box measurement (Bx1.Average), and the minimum of temperature Box measurement (Bx1.Min.), represent the temperature of solar steam (black line), the average temperature of bulk liquid (red line), and the minimum temperature of bulk liquid (blue line), respectively. The curves of steam temperature (a) driven by high concentration of TAP (~5 × 10^{13} photoabsorbers/L) and under high intensity sunlight illumination (779-769 W/m^2)It shows that the high temperature of solar steam mostly range 105 to 110 ℃, and the fast T_b (2.7 s). The whole and rough video with respect to the first period from onset to offset irradiation (0-256 s) was shown in Supplementary Video 2, as well as its temperature distribution in Supplementary Video 3. It shows the whole process of rapidly generating vast solar steam and macroscopic bubbles mingled with explosive whistle. **b**, The capture of IR image shows the temperature distribution in the process of generating solar steam. It shows the huge temperature gradient more than 90 ℃. **c-e**, The average temperature curve of cooling stage and its corresponding Fitting curve (c), (d), and (e) correlates with cooling stage had been marked with the dotted ellipse with green color involving Figure S20a, Figure S21b, and Figure S23a, respectively. **f**, The curves of cooling rate result from the first order derivative calculation correspond to (c-e), the black line, the red line, and the blue line were the curve of cooling rate of (c), (d), and (e), respectively. The curve of cooling rate again the average temperature of buck dispersion can accurately calculate the instant thermal loss of convertor.

Text 3. The instant thermal loss ratio of the convertor on the stage of generating solar steam

The curve of average temperature involving bulk dispersion accurately represents the instant thermal loss of the convertor without irradiation, and the first order derivative curve of average temperature over the average temperature involving bulk dispersion that is the curve of cooling rate as plotted in Figure S23f (Supporting Information). According to the curve of cooling rate and Equation 1, it is possible to accurately calculate the instant thermal loss ratio of the convertor on the stage of generating solar steam.

$$\eta_{\mathrm{L}} = \frac{Q_{\mathrm{L}}}{Q_{\mathrm{I}}} \times 100\% \qquad (1)$$

$$Q_{\mathrm{L}} = \mathrm{m}C_{\mathrm{P}}\mathrm{kdt}; \quad Q_{\mathrm{I}} = I\mathrm{Sdt}$$

Where Q_{L} is the total thermal loss which is the sum of the convective, conductive and radiative heat losses; m is the bulk dispersion weight of TAP, the C_{P} is the heat capacity of water, k is the instant cooling rate, dt is the differential time; Q_{I} is the total input solar energy, which I is the power density of solar irradiation, which S is the optical collection area.

It is reasonable to high average temperature of bulk dispersion correspond to high thermal loss, as shown in curves of average temperature of bulk dispersion (red curve) in Figure S20,S21,S23a (Supporting Information), it was up to 55-60 ℃ under irradiating 3 min, and up to 63-67 ℃ under irradiating 4-5 min. Given without insulation measures of convertor, the curves of average temperature of bulk dispersion Figure S23c-e (Supporting Information) (Figure 8c-e) and corresponding to the curve of cooling rate (Figure S23f, Supporting Information) reveal that η_{L} notably increases when the average temperature of convertor is up to 50-55 ℃, while the average temperature of bulk dispersion is below 50 ℃， k is below -0.15 ℃/s, η_{L} also turns down. The cooling rate curve also reveals that both T_b and k are relative with C_c and the localized solar steam. The better localized solar steam renders the higher η_{e} and the less η_{L}, and that to minimize η_{L}, the average temperature is better not above 50-55 ℃. Here, we quantified the η_{L} according to the intermediate cooling rate curve (the red curve in Figure S23f, Supporting Information) varying the average temperature of bulk convertor. The average temperature of bulk dispersion 45 ℃, 55 ℃, and 60 ℃ correspond to k = -0.068 ℃/s, k = -0.131 ℃/s, and k = -0.163 ℃/s, respectively. According to Equation 3, thus the second case outdoor test under mean intensity of sunlight 910 W/m^2 in Figure 5a, the average temperature of bulk dispersion 45 ℃, 55 ℃, and 60 ℃ correspond to η_{L} = 7.5%, η_{L} = 14.5%, and η_{L} = 18.1%, respectively. Note that, for quickly and accurately evaluate the overall performances of TAP, all the outdoor tests of generating solar steam under sunlight irradiation did not take any insulation measure. To minimize the η_{L}, some accessible methods including maintaining the average temperature below 50-55 ℃ via flowing DI water, combining thermoelectric generators, and covering the insulating layer on external surface of the convertor, are possible to further improve the efficiency.

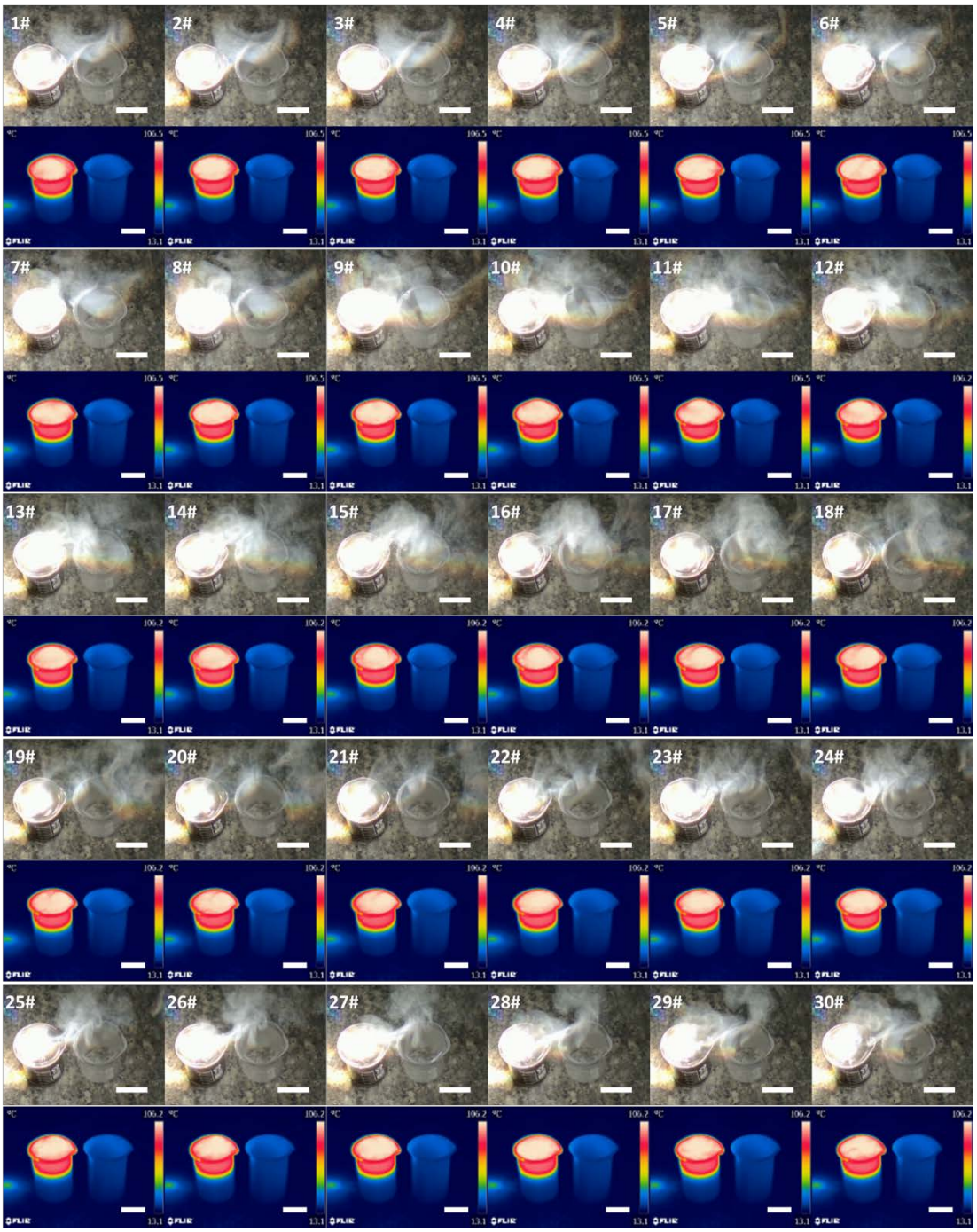

Figure 24. The in-site captures of continuously produce drastic boiling steam in 1 s driven by relative high concentration TAP.

1-30#, The instant capture of generating vast solar steam obviously shows the instant situation of vast steam rapidly released only in the irradiating area involving the interface of liquid-air, as well as the bubbles mingled with explosive whistle. The thermal infrared imaging recorded by IR camera below (1-30#) corresponding the temperature distribution shows the huge temperature gradient (> 90 ℃) and the high temperature of localized solar steam (> 105 ℃). In each outdoor test, the relative high concentration of TAP (III-1#) was ~5×10^{13} photoabsorbers/L, harvesting irradiation area: 35 × 35 cm. In each case, the scale bar is equal to 2 cm.

Video1 (separate file). The macroscopic temperature of hot-spots in terms of TAP.

Video 2 (separate file). Vast and rapid solar steam and macroscopic bubbles accompanying explosive whistle.

Video 3 (separate file). The temperature distribution involving localized and high temperature of solar steam and huge temperature gradient.

References

1. Lucky, Sasidharan Swarnalatha, Khee Chee Soo, and Yong Zhang. "Nanoparticles in photodynamic therapy." *Chemical Reviews* 115.4 (2015): 1990-2042.
2. Hessel, Colin M., et al. "Copper selenide nanocrystals for photothermal therapy." *Nano letters* 11.6 (2011): 2560-2566.
3. Yu, W. William, et al. "Experimental determination of the extinction coefficient of CdTe, CdSe, and CdS nanocrystals." *Chemistry of Materials* 15.14 (2003): 2854-2860.
4. Tian, Qiwei, et al. "Hydrophilic Cu9S5 nanocrystals: a photothermal agent with a 25.7% heat conversion efficiency for photothermal ablation of cancer cells in vivo." *ACS nano*5.12 (2011): 9761-9771.
5. Li, B., Ye, K., Zhang, Y., Qin, J., Zou, R., Xu, K., ... & Hu, J. (2015). Photothermal theragnosis synergistic therapy based on bimetal sulphide nanocrystals rather than nanocomposites. Advanced Materials, 27(8), 1339-1345.
6. Jain, Prashant K., et al. "Calculated absorption and scattering properties of gold nanoparticles of different size, shape, and composition: applications in biological imaging and biomedicine." *The journal of physical chemistry B* 110.14 (2006): 7238-7248.
7. Nikoobakht, Babak, Jianping Wang, and Mostafa A. El-Sayed. "Surface-enhanced Raman scattering of molecules adsorbed on gold nanorods: off-surface plasmon resonance condition." *Chemical Physics Letters* 366.1-2 (2002): 17-23.
8. Hirsch, Leon R., et al. "Nanoshell-mediated near-infrared thermal therapy of tumors under magnetic resonance guidance." *Proceedings of the National Academy of Sciences*100.23 (2003): 13549-13554.
9. Zeng, Jie, et al. "Controlling the shapes of silver nanocrystals with different capping agents." *Journal of the American Chemical Society* 132.25 (2010): 8552-8553.
10. Baffou, Guillaume, and Romain Quidant. "Thermo-plasmonics: using metallic nanostructures as nano-sources of heat." *Laser & Photonics Reviews* 7.2 (2013): 171-187.
11. Jia, Henglei, et al. "Synthesis of absorption-dominant small gold nanorods and their plasmonic properties." *Langmuir*31.26 (2015): 7418-7426.
12. Wang, Shanshan, Hong Xu, and Jian Ye. "Plasmonic rod-in-shell nanoparticles for photothermal therapy." *Physical Chemistry Chemical Physics* 16.24 (2014): 12275-12281.
13. Onal, E. Doruk, and Kaan Guven. "Plasmonic photothermal therapy in third and fourth biological windows." *The Journal of Physical Chemistry C* 121.1 (2017): 684-690.

14. Ogunyankin, Maria O., et al. "Optimizing the NIR fluence threshold for nanobubble generation by controlled synthesis of 10–40 nm hollow gold nanoshells." *Advanced Functional Materials* 28.10 (2018): 1705272.
15. Hogan, Nathaniel J., et al. "Nanoparticles heat through light localization." *Nano letters* 14.8 (2014): 4640-4645.
16. Neumann, Oara, et al. "Solar vapor generation enabled by nanoparticles." *ACS nano* 7.1 (2012): 42-49.
17. Zielinski, Marcin S., et al. "Hollow mesoporous plasmonic nanoshells for enhanced solar vapor generation." *Nano letters*16.4 (2016): 2159-2167.
18. Wang, Hui, et al. "Symmetry breaking in individual plasmonic nanoparticles." *Proceedings of the National Academy of Sciences* 103.29 (2006): 10856-10860.
19. Rycenga, Matthew, et al. "Controlling the synthesis and assembly of silver nanostructures for plasmonic applications." *Chemical reviews* 111.6 (2011): 3669-3712.
20. Jin, Rongchao, et al. "Controlling anisotropic nanoparticle growth through plasmon excitation." *Nature* 425.6957 (2003): 487.
21. Bastús, Neus G., et al. "Synthesis of highly monodisperse citrate-stabilized silver nanoparticles of up to 200 nm: kinetic control and catalytic properties." *Chemistry of Materials* 26.9 (2014): 2836-2846.
22. Bian, Kexin, et al. "Peptide-Directed Hierarchical Mineralized Silver Nanocages for Anti-Tumor Photothermal Therapy." *ACS Sustainable Chemistry & Engineering* 6.6 (2018): 7574-7588.
23. Link, Stephan, and Mostafa A. El-Sayed. "Size and temperature dependence of the plasmon absorption of colloidal gold nanoparticles." *The Journal of Physical Chemistry B* 103.21 (1999): 4212-4217.
24. Huang, Ping-Ji, et al. "Nanoaggregate-Embedded Beads as Novel Raman Labels for Biodetection." *Advanced Functional Materials* 19.2 (2009): 242-248.
25. Huang, Xiaohua, and Mostafa A. El-Sayed. "Gold nanoparticles: optical properties and implementations in cancer diagnosis and photothermal therapy." *Journal of advanced research* 1.1 (2010): 13-28.
26. Huang, Xiaohua, et al. "Cancer cell imaging and photothermal therapy in the near-infrared region by using gold nanorods." *Journal of the American Chemical Society* 128.6 (2006): 2115-2120.
27. Skrabalak, Sara E., et al. "Facile synthesis of Ag nanocubes and Au nanocages." *Nature protocols* 2.9 (2007): 2182.
28. Navarro, Julien RG, et al. "Synthesis of PEGylated gold nanostars and bipyramids for intracellular uptake." *Nanotechnology* 23.46 (2012): 465602.
29. Xie, Jianping, et al. "The synthesis of SERS-active gold nanoflower tags for in vivo applications." *ACS nano* 2.12 (2008): 2473-2480.
30. Huang, Peng, et al. "Triphase interface synthesis of plasmonic gold bellflowers as near-infrared light mediated acoustic and thermal theranostics." *Journal of the American Chemical Society* 136.23 (2014): 8307-8313.
31. Kim, Jun-Hyun, and T. Randall Lee. "Hydrogel-templated growth of large gold nanoparticles: synthesis of thermally responsive hydrogel− nanoparticle composites." *Langmuir*23.12 (2007): 6504-6509.

32. Song, Jibin, Jiajing Zhou, and Hongwei Duan. "Self-assembled plasmonic vesicles of SERS-encoded amphiphilic gold nanoparticles for cancer cell targeting and traceable intracellular drug delivery." *Journal of the American Chemical Society* 134.32 (2012): 13458-13469.
33. Goodman, Amanda M., et al. "The surprising in vivo instability of near-IR-absorbing hollow Au–Ag nanoshells." *ACS nano*8.4 (2014): 3222-3231.
34. Nagy-Simon, Timea, et al. "Antibody Conjugated, Raman Tagged Hollow Gold–Silver Nanospheres for Specific Targeting and Multimodal Dark-Field/SERS/Two Photon-FLIM Imaging of CD19 (+) B Lymphoblasts." *ACS applied materials & interfaces* 9.25 (2017): 21155-21168.
35. R. Daniel, Josée, et al. "Gold Speciation and Co-reduction Control the Morphology of AgAu Nanoshells in Formaldehyde-Assisted Galvanic Replacement." *The Journal of Physical Chemistry C* 122.31 (2018): 18168-18176.
36. Shakiba, Amin, et al. "Silver-free gold nanocages with near-infrared extinctions." *ACS Omega* 1.3 (2016): 456-463.
37. Pande, Surojit, et al. "Synthesis of normal and inverted gold− silver core− shell architectures in β-cyclodextrin and their applications in SERS." *The Journal of Physical Chemistry C*111.29 (2007): 10806-10813.
38. Godfrey, Ian J., et al. "Structure of Gold–Silver Nanoparticles." *The Journal of Physical Chemistry C* 121.3 (2017): 1957-1963.
39. Bu, Yanru, and Sangwha Lee. "Influence of dopamine concentration and surface coverage of Au shell on the optical properties of Au, Ag, and AgcoreAushell nanoparticles." *ACS applied materials & interfaces* 4.8 (2012): 3923-3931.
40. Li, Chien-Hung, et al. "Plasmonically Enhanced Photocatalytic Hydrogen Production from Water: The Critical Role of Tunable Surface Plasmon Resonance from Gold–Silver Nanoshells." *ACS applied materials & interfaces* 8.14 (2016): 9152-9161.
41. Wang, Zhuyuan, et al. "SERS-fluorescence joint spectral encoding using organic–metal–QD hybrid nanoparticles with a huge encoding capacity for high-throughput biodetection: putting theory into practice." *Journal of the American Chemical Society* 134.6 (2012): 2993-3000.
42. Rycenga, Matthew, et al. "Probing the surface-enhanced Raman scattering properties of Au–Ag nanocages at two different excitation wavelengths." *Physical Chemistry Chemical Physics* 11.28 (2009): 5903-5908.
43. Chen, Jingyi, et al. "Facile synthesis of gold− silver nanocages with controllable pores on the surface." *Journal of the American Chemical Society* 128.46 (2006): 14776-14777.
44. Yan, Yong, et al. "Mesoscopically Bi-continuous Ag–Au Hybrid Nanosponges with Tunable Plasmon Resonances as Bottom-Up Substrates for Surface-Enhanced Raman Spectroscopy." *Chemistry of Materials* 28.21 (2016): 7673-7682.
45. Dantham, V. R., et al. "Taking whispering gallery-mode single virus detection and sizing to the limit." *Applied Physics Letters*101.4 (2012): 043704.
46. Schwartzberg, Adam M., et al. "Synthesis, characterization, and tunable optical properties of hollow gold nanospheres." *The Journal of Physical Chemistry B* 110.40 (2006): 19935-19944.
47. Zielinski, Marcin S., et al. "Hollow mesoporous plasmonic nanoshells for enhanced solar vapor generation." Nano letters 16.4 (2016): 2159-2167.

48. Lindley, Sarah A., et al. "Highly Tunable Hollow Gold Nanospheres: Gaining Size Control and Uniform Galvanic Exchange of Sacrificial Cobalt Boride Scaffolds." *ACS applied materials & interfaces* 10.15 (2018): 12992-13001.
49. Shi, Weili, et al. "Gold nanoshells on polystyrene cores for control of surface plasmon resonance." *Langmuir* 21.4 (2005): 1610-1617.
50. Li, Chien-Hung, et al. "In situ growth of hollow gold–silver nanoshells within porous silica offers tunable plasmonic extinctions and enhanced colloidal stability." *ACS applied materials & interfaces* 6.22 (2014): 19943-19950.
51. Caruso, Frank, et al. "Multilayer Assemblies of Silica-Encapsulated Gold Nanoparticles on Decomposable Colloid Templates." *Advanced Materials* 13.14 (2001): 1090-1094.
52. Kim, Jun-Hyun, et al. "Gold, palladium, and gold− palladium alloy nanoshells on silica nanoparticle cores." *ACS applied materials & interfaces* 1.5 (2009): 1063-1069.
53. Lal, Surbhi, Stephan Link, and Naomi J. Halas. "Nano-optics from sensing to waveguiding." *Nature photonics* 1.11 (2007): 641.
54. Asadirad, Amir M., and Neil R. Branda. "Two Colors of Light Are Needed to Break Bonds and Release Small Molecules from the Surface of SiO_2–Au Core–Shell Nanoparticles." *Journal of the American Chemical Society* 137.8 (2015): 2824-2827.
55. Vongsavat, Varadee, et al. "Ultrasmall hollow gold–silver nanoshells with extinctions strongly red-shifted to the near-infrared." *ACS applied materials & interfaces* 3.9 (2011): 3616-3624.
56. Yang, Peipei, et al. "Encapsulated silver nanoparticles can be directly converted to silver nanoshell in the gas phase." *Nano letters* 15.12 (2015): 8397-8401.
57. Li, Ju-Mei, et al. "Poly (styrene-co-acrylic acid) core and silver nanoparticle/silica shell composite microspheres as high performance surface-enhanced Raman spectroscopy (SERS) substrate and molecular barcode label." *Journal of Materials Chemistry* 21.16 (2011): 5992-5998.
58. Moaseri, Ehsan, et al. "Reversible self-assembly of glutathione-coated gold nanoparticle clusters via pH-tunable interactions." *Langmuir* 33.43 (2017): 12244-12253.
59. Wang, Hui, et al. "Symmetry breaking in individual plasmonic nanoparticles." *Proceedings of the National Academy of Sciences* 103.29 (2006): 10856-10860.
60. Hu, Ying, Sterling J. Noelck, and Rebekah A. Drezek. "Symmetry breaking in gold− silica− gold multilayer nanoshells." *Acs Nano* 4.3 (2010): 1521-1528.
61. Mukherjee, Shaunak, et al. "Fanoshells: nanoparticles with built-in Fano resonances." *Nano letters* 10.7 (2010): 2694-2701.
62. Fan, Jonathan A., et al. "Self-assembled plasmonic nanoparticle clusters." *science* 328.5982 (2010): 1135-1138.
63. Lee, Jaewon, and Du-Jeon Jang. "Highly efficient catalytic performances of eco-friendly grown silver nanoshells." *The Journal of Physical Chemistry C* 120.7 (2016): 4130-4138.
64. Höller, Roland PM, et al. "Protein-assisted assembly of modular 3D plasmonic raspberry-like core/satellite nanoclusters: correlation of structure and optical properties." *ACS nano* 10.6 (2016): 5740-5750.

65. Halder, Aditi, and N. Ravishankar. "Ultrafine single-crystalline gold nanowire arrays by oriented attachment." *Advanced Materials* 19.14 (2007): 1854-1858.
66. Manna, Uttam, et al. "Selective induction of optical magnetism." *Nano letters* 17.12 (2017): 7196-7206.
67. Song, Jibin, et al. "Rational design of branched nanoporous gold nanoshells with enhanced physico-optical properties for optical imaging and cancer therapy." *ACS nano* 11.6 (2017): 6102-6113.
68. Yang, Longkun, et al. "Polarization state of light scattered from quantum plasmonic dimer antennas." *ACS nano* 10.1 (2015): 1580-1588.
69. Lassiter, J. Britt, et al. "Close encounters between two nanoshells." *Nano letters* 8.4 (2008): 1212-1218.
70. Tsai, Ming-Fong, et al. "Au nanorod design as light-absorber in the first and second biological near-infrared windows for in vivo photothermal therapy." *ACS nano* 7.6 (2013): 5330-5342.
71. Zhang, Qiao, et al. "Tailored synthesis of superparamagnetic gold nanoshells with tunable optical properties." *Advanced Materials* 22.17 (2010): 1905-1909.
72. He, Jie, et al. "Self-assembly of amphiphilic plasmonic micelle-like nanoparticles in selective solvents." *Journal of the American Chemical Society* 135.21 (2013): 7974-7984.
73. Stöber, Werner, Arthur Fink, and Ernst Bohn. "Controlled growth of monodisperse silica spheres in the micron size range." *Journal of colloid and interface science* 26, no. 1 (1968): 62-69.
74. Sun, Yugang, and Younan Xia. "Shape-controlled synthesis of gold and silver nanoparticles." *science* 298.5601 (2002): 2176-2179.
75. Wang, Zhuang, et al. "Facile synthesis of monodisperse silver nanoparticles for screen printing conductive inks." *Journal of Materials Science: Materials in Electronics* 28.22 (2017): 16939-16947.